# Simulation of trace structure formation via PHITS for the nanoscale deposition of electron beams in FLASH Radiotherapy.
# Track-structure modeling using PHITS and TOPAS-nBio code extensions

Lic. Kendry Antúnez Campañá[1], Supervisor Dr. Iván Padrón Díaz[2]
[1]Radiation Damage Laboratory, Center for Technological Applications and Nuclear Development, Havana, Cuba.
[2]Laboratory of Radiation Biology, Joint Institute for Nuclear Research, Russia.
e-mail: antunez.kendry@gmail.com, padron@jinr.ru

*Abstract* – **FLASH radiotherapy, characterized by ultra-high dose rates, reduces toxicity in healthy tissue without compromising tumor control, although its radiochemical mechanisms at the subcellular scale remain under debate. This work employs Monte Carlo simulations using the PHITS code in its track-structure modality to analyze the energy deposition of electrons (1–40 keV) in nanometric volumes (5–100 nm). We investigate the influence of pulse duration (10 ns–100 ns) and beam energy on the production kinetics of reactive species and the formation of ionization clusters. Preliminary results from dose_vs_time and ioniz_cluster analyses allow the quantification of differences in the density of energy deposition events and secondary electron escape, laying the groundwork for a mechanistic comparison between FLASH and conventional radiotherapy (CONV). This multi-scale approach is crucial for validating the hypotheses of local oxygen depletion and differential DNA damage under normoxic and hypoxic conditions.**

*Keywords* – **FLASH radiotherapy, PHITS, Monte Carlo simulation, ultra-high dose rate, normal tissue sparing, computational dosimetry**

## NOMENCLATURE

| | |
|---|---|
| CONV | Conventional radiotherapy. |
| CPE | Charged particle equilibrium. |
| CSDA | Continuous slowing-down approximation. |
| FLASH-RT | FLASH radiotherapy. |
| LET | Linear energy transfer. |
| LMDS | Locally multiply damaged site. |
| PHITS | Particle and Heavy Ion Transport code System. |
| ROS | Reactive oxygen species. |
| UHDR | Ultra-high dose rate. |

## I. INTRODUCTION

The clinical translation of FLASH radiotherapy (FLASH-RT) faces a fundamental knowledge gap: the causal relationship between ultra-high dose rates (UHDR) and the mechanisms of healthy tissue preservation is not fully elucidated at the molecular level. Although the hypotheses of hypoxia induced by oxygen depletion and free radical recombination are predominant, most current radiobiological models lack the necessary spatial (nanometric) and temporal (nanosecond) resolution to accurately describe the topology of DNA damage and the early chemical kinetics in the immediate vicinity of the ionization track (7; 10). There is a critical need to quantify how specific physical parameters of the pulsed beam—such as the energy of secondary electrons (below 50 keV) and the pulse duration—modulate the formation of complex damage clusters in subcellular structures with dimensions comparable to chromatin (5–100 nm). Without this mechanistic bridge between the physics of radiation-matter interaction and damage biology, the safe optimization of FLASH protocols remains empirical (8).

### *A. Hypothesis*

The application of ultra-short (nanosecond scale) and low-energy (1–40 keV) electron pulses modifies the stochastic distribution of energy deposition at the nanoscale compared to equivalent continuous irradiation. Specifically, we postulate that:

1. The temporal dynamics of the pulse alter the production efficiency of reactive oxygen species (ROS) due to the competition between ionization events and electronic escape processes (escape_vs_time).
2. The variation of the incident beam energy modifies the Linear Energy Transfer (LET) and, consequently, the complexity of ionization clusters (ioniz_cluster), differentially impacting damage reparability in biologically relevant volumes (50–100 nm).

### *B. General Objective*

To evaluate the impact of electron beam physical parameters (energy and pulse duration) on nanoscale energy deposition patterns and early ionization kinetics, using the PHITS track-structure code as a platform to discern between the radiobiological effects of FLASH-RT and conventional radiotherapy (CONV-RT).

### *C. Specific Objectives*

1. **Temporal Characterization:** Analyze the evolution of deposited dose (dose_vs_time) and electron fluence for pulse configurations of 10 ns, 50 ns, and 100 ns, identifying charged particle equilibrium (CPE) regimes in geometries ranging from 5 to 100 nm.
2. **Stochastic Microdosimetry Analysis:** Compare histograms of energy deposited per event (edep_hist) and ionization cluster spectra (ioniz_cluster) for incident energies of 1 keV, 10 keV, and 40 keV, correlating the resulting LET (let_water) with the probability of complex damage.
3. **Quantification of Electronic Escape:** Determine the fraction of energy leaving the nanometric volume of

interest as a function of beam energy (escape_vs_time), a critical factor for modeling dose deposition in cellular organelles.

4. **Validation of Track Models:** Establish a baseline of simulated radiolytic yields (G-values) for the physicochemical phase, preparing the computational environment for the future introduction of oxygen chemical reactions and DNA geometric structures (objectives of subsequent project stages).

## II. THEORETICAL FRAMEWORK

The growing interest in understanding the macroscopic behavior of radiation when ultra-high dose rates are applied in radiotherapy—a modality known as FLASH-RT—has driven the development of track-structure models within general-purpose transport codes (4; 9). These models, employed in fields as diverse as radiation biology, radiotherapy, semiconductor technologies, and detector physics, enable an unprecedented level of detail. By explicitly using cross sections for each energy deposition event associated with atomic interactions, track-structure calculations achieve sub-micron spatial resolution and sub-keV energy resolution (10). In this context, the present work focuses on the computer simulation of radiolytic yields for the main chemical species generated at the cellular scale, as well as the resulting biological damage, with the aim of comparing the effects of FLASH radiotherapy and conventional radiotherapy under different oxygen concentrations. This analysis will rely on the advanced capabilities of the PHITS transport code, the fundamentals and applications of which in emerging therapies are detailed below.

### *A. FLASH Radiotherapy*

Radiotherapy (RT) is an essential tool in cancer treatment, where the balance between tumor destruction and preservation of surrounding healthy tissue is critical for improving patient quality of life. Traditionally, this toxicity is reduced through dose fractionation, allowing healthy tissue recovery, and through technological advances in precise radiation delivery (5). FLASH radiotherapy is an innovative modality that delivers ultra-high dose rates (UHDR) in extremely short times (milliseconds), with the potential to significantly decrease toxicity in normal tissues without sacrificing antitumor efficacy (1; 6). In vitro and in vivo studies show a reduction in acute and late damage in normal tissues irradiated with FLASH compared to conventional radiotherapy (CONV), while maintaining tumor control in various animal models (4; 9).

From a radiobiological perspective, three main mechanisms have been proposed to explain this differential effect:

- **Local oxygen depletion (Induced hypoxia hypothesis):** Ultra-rapid irradiation may consume oxygen in healthy tissue during the instantaneous radiation delivery, creating a temporarily hypoxic environment that limits the generation of reactive free radicals responsible for damage (2; 6).
- **Differential DNA damage:** Studies suggest that FLASH radiation induces a lower amount or complexity of DNA damage in healthy tissues, possibly due to rapid recombination of peroxyl radicals, resulting in reduced genotoxic stress (7; 8).
- **Modulated immune response:** FLASH radiotherapy could alter the local and systemic immune response, reducing inflammation and senescence in normal tissues while maintaining or even enhancing tumor immunogenicity (9).

The tumor microenvironment and the interaction with circulating and immune cells represent another key dimension that remains poorly understood, especially in humans, and is an active area of research to better comprehend the safety and clinical efficacy of FLASH RT (10).

Regarding application with electron beams, although most preclinical studies are conducted with electrons or protons at clinical energies, the exploration of energies as low as 4 keV opens new perspectives in understanding the physical and chemical effects on biomolecules and cells, particularly considering the peculiarities in free radical formation and recombination as well as beam penetration (2; 6). However, to date, the clinical translation of FLASH RT still faces technical challenges and requires rigorous studies to establish safe and effective protocols (1).

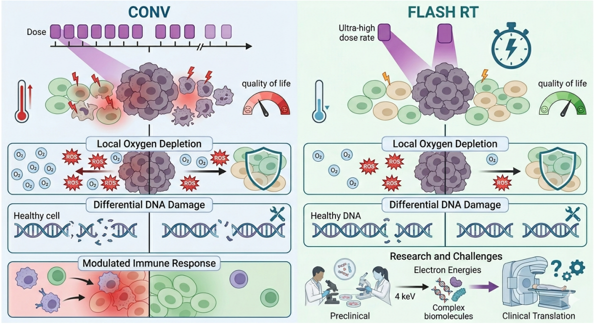

Fig. 1. Schematic overview of FLASH radiotherapy principles. FLASH delivers ultra-high dose rates (UHDR) in millisecond pulses, significantly reducing normal tissue toxicity while preserving antitumor efficacy. Proposed radiobiological mechanisms include local oxygen depletion inducing transient hypoxia, differential DNA damage complexity favoring normal tissue repair, and modulation of the immune response to reduce inflammation and senescence. Despite promising preclinical results, clinical translation requires further technical and safety validation.

### *B. PHITS Monte Carlo Code*

The PHITS system (Particle and Heavy Ion Transport code System) is a widely used Monte Carlo simulation package for modeling particle transport and the interaction of radiation with materials and biological tissues at both microscopic and macroscopic levels (3; 11). This code is based on fundamental principles of nuclear and particle physics, calculating in a probabilistic manner the interaction events (such as scattering, absorption, and nuclear reactions) of protons, neutrons, alpha particles, and other heavy ions with matter.

PHITS employs nuclear interaction theories and radiation physics, including nuclear cross-sections, collision models, and secondary particle emission, which enables accurate estimation of particle production and propagation within complex biological systems (3; 12). Simulations with PHITS can record not only the deposited dose but also specific radiation events at the cellular scale, such as the number of alpha particle hits in the nucleus or cytoplasm, which is crucial for understanding DNA damage (11).

In the context of Flash radiotherapy—an emerging modality that uses high radiation doses in ultra-short times to maximize tumor damage while minimizing effects on healthy tissue—PHITS is an indispensable tool. Its ability to model radiation interactions in detail at the cellular level allows exploration of damage mechanisms and optimization of irradiation parameters, helping to quantify specific biological effects and adapt protocols to maximize therapeutic efficacy (12; 13).

In particular, the application of PHITS in advanced therapy studies such as proton-boron fusion has demonstrated that material distributions (such as boron concentration and distribution within cells) can be simulated, and the energy contribution from high-LET (linear energy transfer) alpha particles can be examined. These particles cause highly localized and effective damage at the level of tumor DNA (13). This contributes to a deep and quantitative understanding that goes beyond simple average dose evaluation, which is essential for the development and assessment of modalities such as Flash radiotherapy and other emerging therapies.

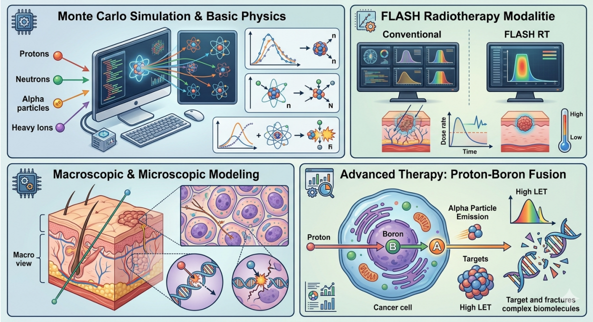

Fig. 2. Overview of PHITS Monte Carlo capabilities for advanced radiotherapy. Left panel: Schematic representation of particle transport (protons, neutrons, alpha particles, and heavy ions) and the comparison of conventional radiotherapy versus FLASH-RT, highlighting the ultra-high dose rate delivered in a short time pulse to spare healthy tissue. Right panel: Simulation of Proton-Boron Fusion therapy, where the capture reaction generates high-LET alpha particles within the tumor cell. PHITS enables the microscopic tracking of these particles to quantify localized DNA damage and nuclear fragmentation, providing a mechanistic understanding beyond macroscopic dose deposition.

## III. MATERIALS AND METHODS

### *A. Monte Carlo Transport and Track-Structure Physics*

All simulations were performed with the Particle and Heavy Ion Transport code System (PHITS) version 3.02 (3), operating in its event-by-event track-structure mode. In this mode each inelastic collision of an electron with a water molecule is treated individually, using energy-dependent differential cross sections for ionisation, electronic excitation, and elastic scattering (12). The physical stage follows the electron cascade down to a kinetic energy of 1 eV, at which point the residual energy is deposited locally. The subsequent physico-chemical and chemical stages (up to 1 $\mu$s) employ the standard radiolysis model of water, which includes 14 reactive species and more than 40 chemical reactions (11). The user-defined runtime parameters that control the accuracy of the transport are summarised in Algorithms 1 and 2.

### *B. Geometrical Model and Irradiation Conditions*

The biological target is modelled as a liquid-water sphere of radius $r$ (variable from 5 nm to 100 nm), centred at the origin and surrounded by a shell of dry air (ICRU composition) extending to 10 $\mu$m (Fig. 3). The water density is set to 1.0 g/cm$^3$ and the air density to $1.205 \times 10^{-3}$ g/cm$^3$. A parallel, mono-energetic electron beam is emitted from a plane at $z = -20$ nm, directed along the $+z$ axis and uniformly illuminating the entire sphere. Four incident energies were considered: 1, 4, 10, and 40 keV. The time structure of the beam is a single 50 ns rectangular pulse followed by a 10 ms quiet period; $10^4$ primary electrons are transported in each of 10 batches. This configuration reproduces the ultra-high dose rates characteristic of FLASH radiotherapy while keeping the computational cost manageable.

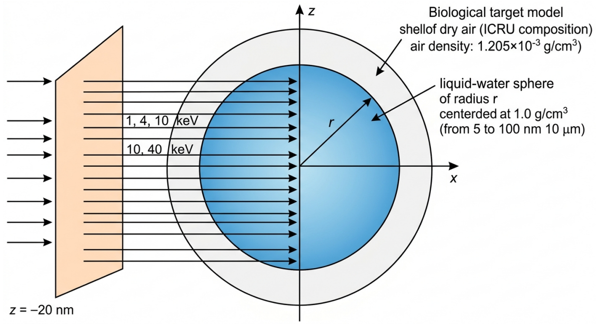

Fig. 3. Simulation geometry: water nanosphere surrounded by air. The electron beam enters from the left ($z < 0$) and deposits energy inside the sphere.

### *C. Scoring Routines and Extracted Observables*

A comprehensive set of physical, physico-chemical, and chemical quantities was accumulated in the water sphere (region 1). Algorithms 1 and 2 list the main scoring commands as they appear in the PHITS input file, together with the corresponding output observables. All tallies are normalised per source electron, allowing direct comparison across different energies and sphere sizes.

- **Macroscopic dose descriptors:** Cumulative dose (`dose_mean_Gy`) and dose vs. time (`dose_vs_time`) give the total energy deposition and confirm the instantaneous nature of the FLASH pulse.
- **Radiation field characterisation:** Spectral electron fluence (`electron_fluence`) and the track projection in the $XZ$ plane (`track_xyz-xz`) visualise the density and spatial distribution of primary and secondary electrons.
- **Microdosimetric quantities:** Histograms of single energy-deposition events (`edep_hist`) and dose-weighted LET distributions (`let_water`) resolve the stochastic nature of energy deposition at the nanometre scale.
- **Clustering and temporal evolution:** The probability of forming clusters of ionisations (`ioniz_cluster`), electronic excitations (`eexc_cluster`), and transient biological species (`tsbio_cluster`) is recorded

event by event. Their time-resolved counterparts (`ioniz_vs_time`, `eexc_vs_time`, `tsbio_vs_time`) capture the reaction kinetics.

- **Electron escape:** The fraction of electrons that leave the sphere without being thermalised (`cutoff_vs_time`) and the energy carried away by escaping particles (`escape_vs_time`) are both tracked.

**Algorithm 1** PHITS track-structure simulation setup.

```
Control: maxcas = 10000, maxbch = 10, istdev = 2
Transport: negs = 1, e-mode = 1, track-structure enabled
Energy cut-offs: emin(12-14) = 1.0E-3 MeV, etsmin = 1.0E-6 MeV
Materials: water ($H_2O$, $\rho = 1.0$ g/cm$^3$), air (ICRU, $\rho = 1.205$E-3 g/cm$^3$)
Geometry:
    Surface 10: sph (0,0,0) 1.0E-6 cm ;    ▷ water sphere of radius $r$
    Surface 999: so 1.0E-3 cm
    Cell 1: inside sphere, water ; Cell 2: air shell ; Cell 999: void
Source: parallel electron beam, $E$ = {1, 4, 10, 40} keV
    s-type = 3, dir = 1.0, phi = 0.0
    Pulse: t-type = 2, tn = 10, tw = 50.0 ns, td = 100 $\mu$s
```

**Algorithm 2** PHITS event loop and post-processing tallies.

```
for all events do
    Transport primary and all secondaries (electron, photon, etc.)
    At each collision in water sphere:
        Update deposited energy, fluence, LET, ionisation/excitation positions
    if simulation time $\leq$ pulse duration then
        Record time-stamped events for dose_vs_time, ioniz_vs_time, ...
    end if
end for
Post-processing tallies:
    [t-deposit] → dose_mean_Gy, dose_vs_time, edep_hist
    [t-track] → electron_fluence
    [T-Track] → track_xyz-xz
    [t-let] → let_water
    [t-interact] → ioniz_cluster, eexc_cluster, tsbio_cluster
    [t-interact, axis=t] → ioniz_vs_time, eexc_vs_time, tsbio_vs_time
    [t-time] → cutoff_vs_time, escape_vs_time
```

## IV. RESULTS

### *A. Temporal Evolution of Absorbed Dose*

The temporal profile of absorbed dose is a fundamental descriptor of the irradiation regime, especially when comparing conventional (CONV) and FLASH dose rates. The dose_vs_time data set captures the cumulative dose deposition over the entire simulation time window, allowing for the identification of the instantaneous dose rate and the duration of the radiation pulse.

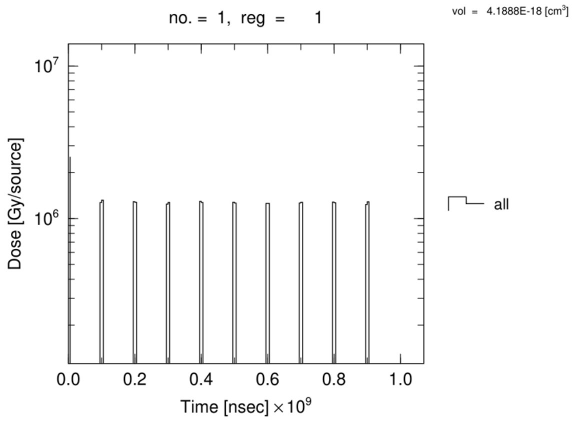

Fig. 4. 1 keV, 10 nm radius. Temporal evolution of absorbed dose.

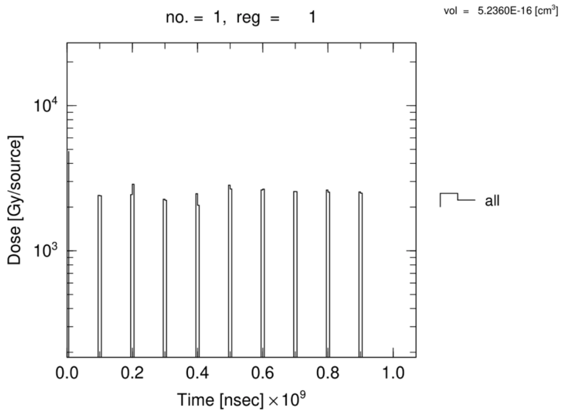

Fig. 5. 1 keV, 50 nm radius. Temporal evolution of absorbed dose.

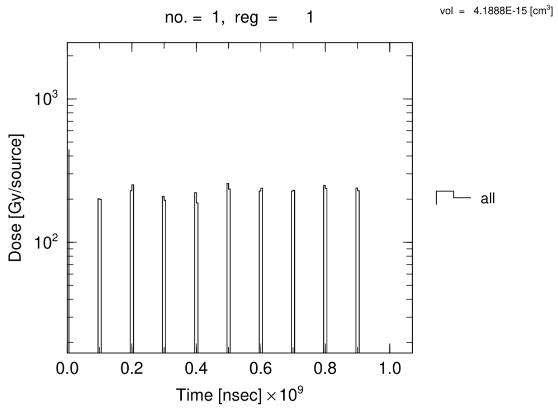

Fig. 6. 1 keV, 100 nm radius. Temporal evolution of absorbed dose.

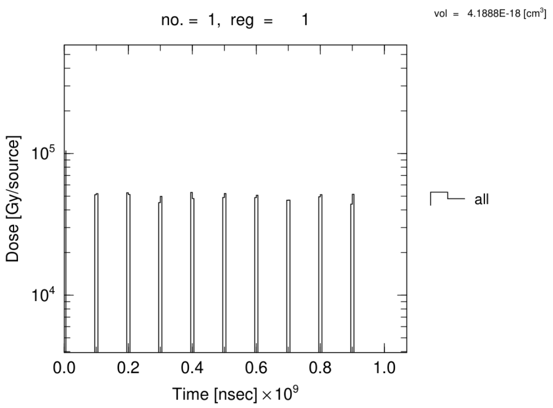

Fig. 7. 4 keV, 10 nm radius. Temporal evolution of absorbed dose.

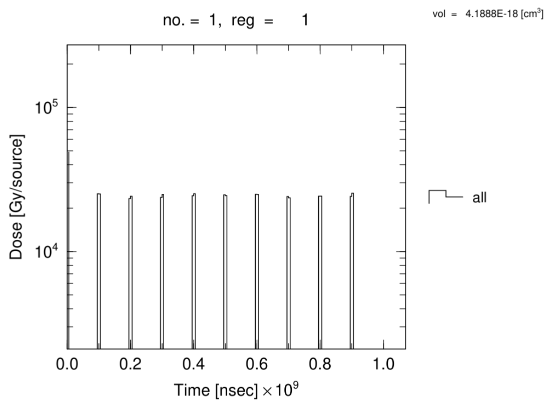

Fig. 10. 10 keV, 10 nm radius. Temporal evolution of absorbed dose.

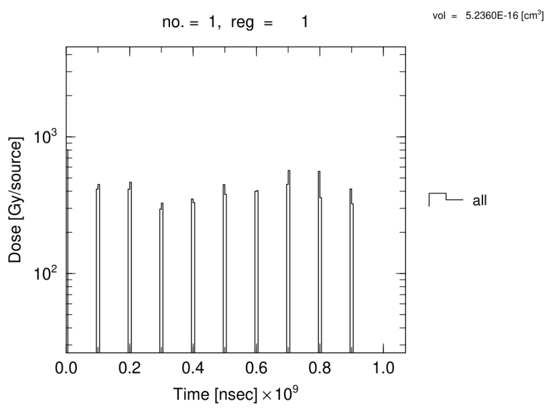

Fig. 8. 4 keV, 50 nm radius. Temporal evolution of absorbed dose.

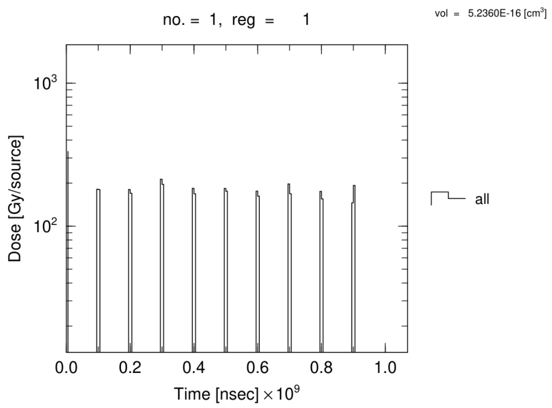

Fig. 11. 10 keV, 50 nm radius. Temporal evolution of absorbed dose.

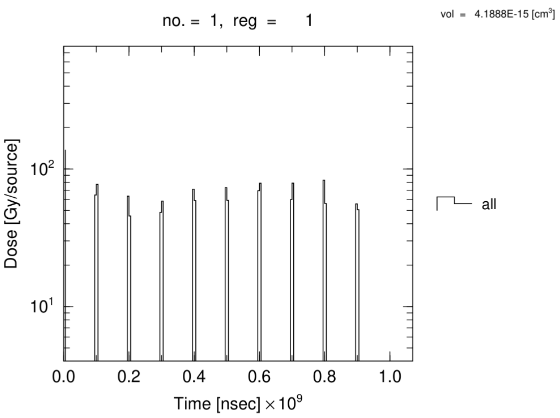

Fig. 9. 4 keV, 100 nm radius. Temporal evolution of absorbed dose.

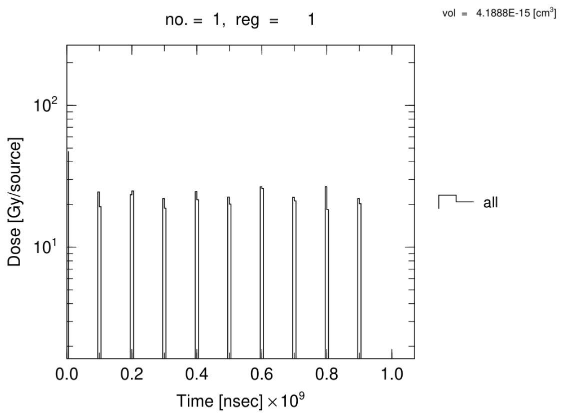

Fig. 12. 10 keV, 100 nm radius. Temporal evolution of absorbed dose.

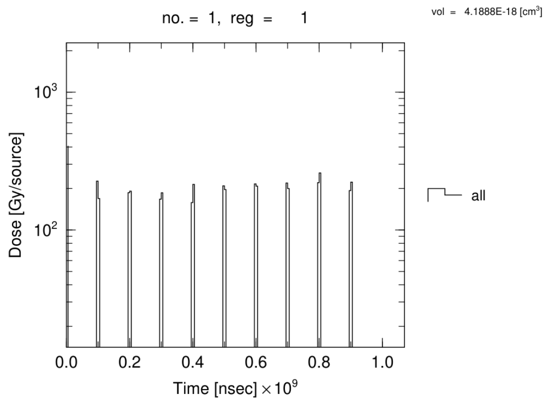

Fig. 13. 40 keV, 10 nm radius. Temporal evolution of absorbed dose.

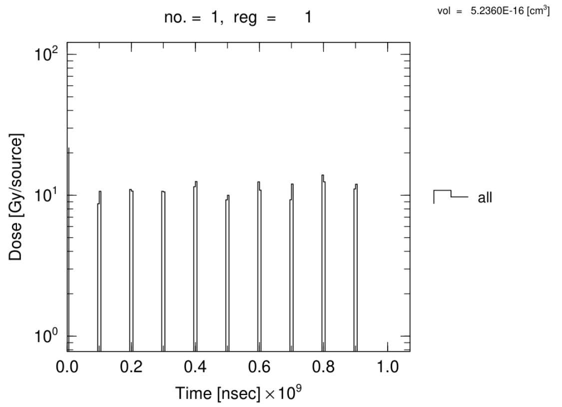

Fig. 14. 40 keV, 50 nm radius. Temporal evolution of absorbed dose.

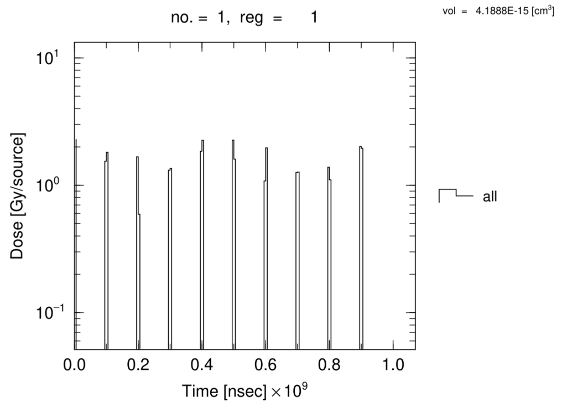

Fig. 15. 40 keV, 100 nm radius. Temporal evolution of absorbed dose.

Figures 4 to 15 show that for all twelve combinations of electron energy and sphere radius, the cumulative dose rises abruptly from zero to a constant plateau within a single time step of 0.02 ns, which is shorter than the 50 ns pulse width. This confirms that the entire energy of the primary electrons is transferred to the water sphere during the FLASH pulse and that no post-pulse dose accumulation occurs from thermalization of secondary electrons. The plateau value thus represents the total energy deposited per source electron. The dose per source decreases monotonically with increasing sphere radius, from $\sim 10^5$ Gy/source at 10 nm to $\sim 10^2$ Gy/source at 100 nm for 1 keV electrons (see Figs. 4–6). This $r^{-3}$ dependence is consistent with the uniform energy deposition assumption for low-energy electrons that stop completely within the target. At 4 and 10 keV, the dose values remain nearly identical to the 1 keV case for the same sphere radii (Figs. 7–12), indicating that these energies are also fully absorbed. At 40 keV, however, the dose plateaus in the 10 nm sphere (Fig. 13) show slight fluctuations and a marginally lower mean value, suggesting electron escape, corroborated by the CSDA range of 40 keV electrons in water ($\approx 7.5$ $\mu$m), much larger than the sphere diameter.

### B. Electron Fluence

The fluence of primary and secondary electrons is a key parameter for characterizing the radiation field, particularly in electron-based FLASH irradiations. The electron_fluence value determines the probability of track overlap—a phenomenon hypothesized to be critical for the FLASH effect.

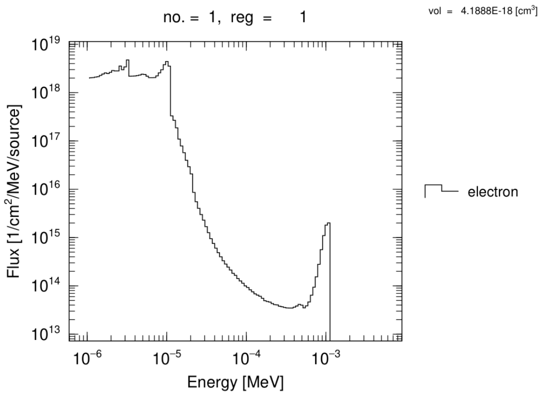

Fig. 16. 1 keV, 10 nm radius. Electron fluence energy spectrum.

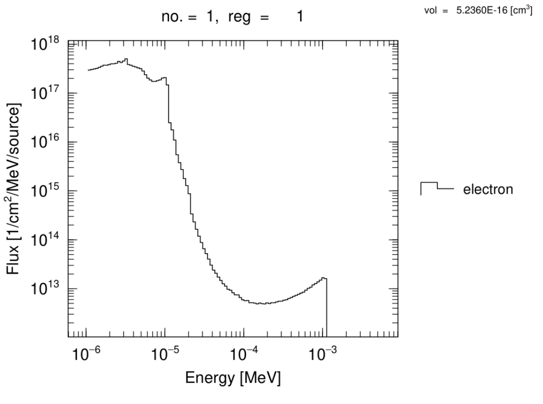

Fig. 17. 1 keV, 50 nm radius. Electron fluence spectrum.

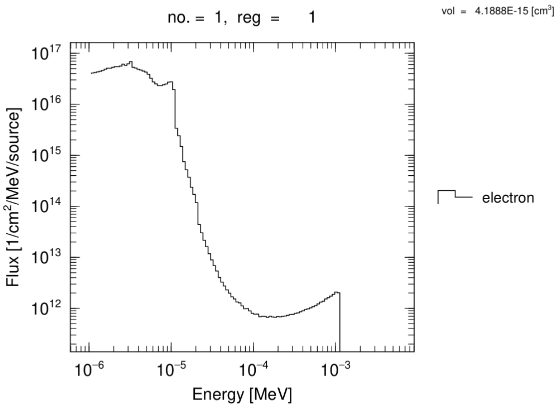

Fig. 18. 1 keV, 100 nm radius. Electron fluence spectrum.

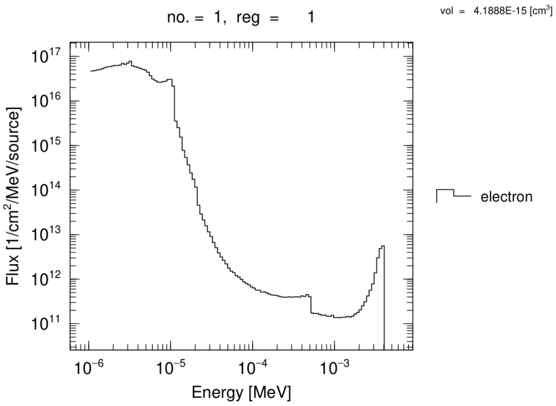

Fig. 21. 4 keV, 100 nm radius. Electron fluence spectrum.

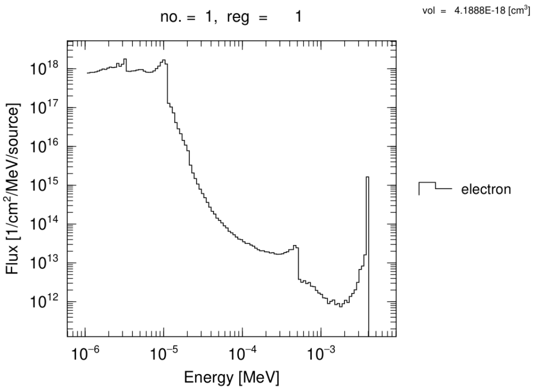

Fig. 19. 4 keV, 10 nm radius. Electron fluence spectrum.

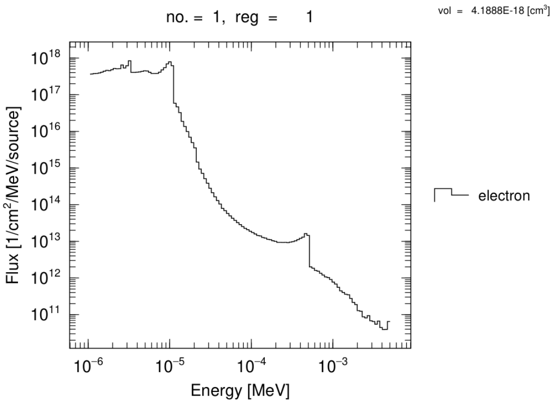

Fig. 22. 10 keV, 10 nm radius. Electron fluence spectrum.

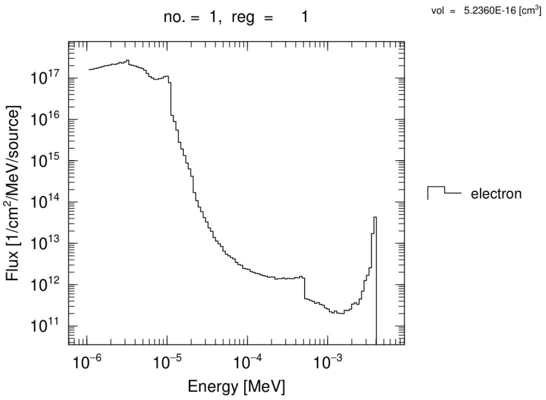

Fig. 20. 4 keV, 50 nm radius. Electron fluence spectrum.

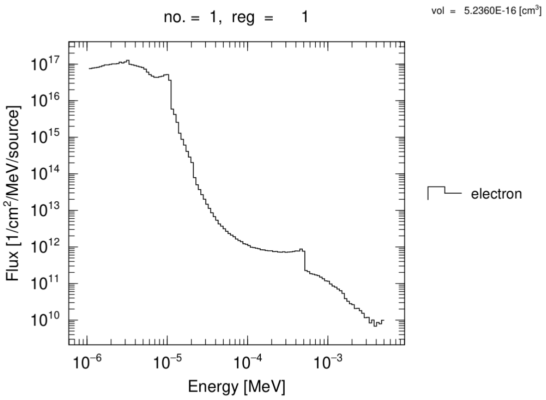

Fig. 23. 10 keV, 50 nm radius. Electron fluence spectrum.

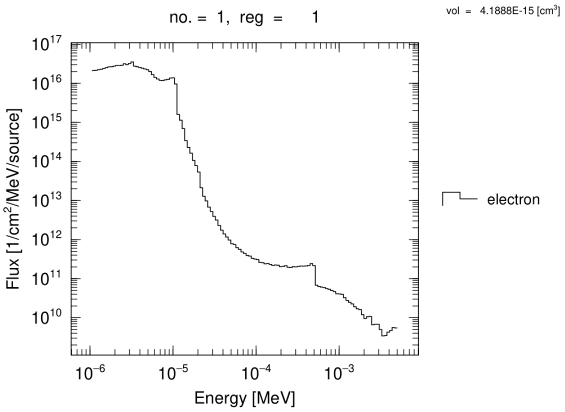

Fig. 24. 10 keV, 100 nm radius. Electron fluence spectrum.

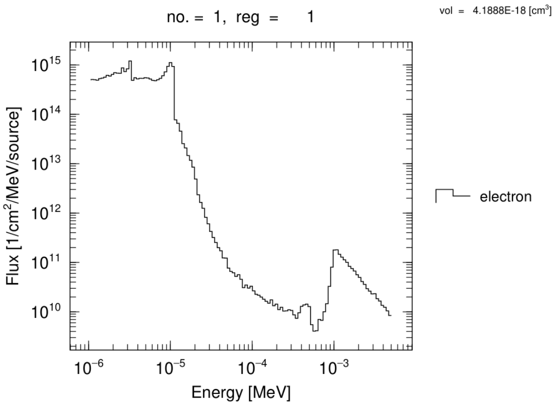

Fig. 25. 40 keV, 10 nm radius. Electron fluence spectrum.

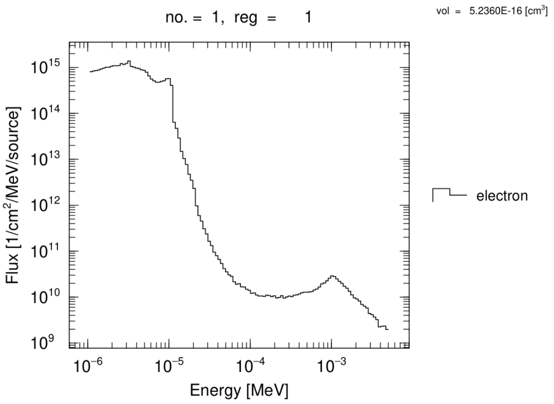

Fig. 26. 40 keV, 50 nm radius. Electron fluence spectrum.

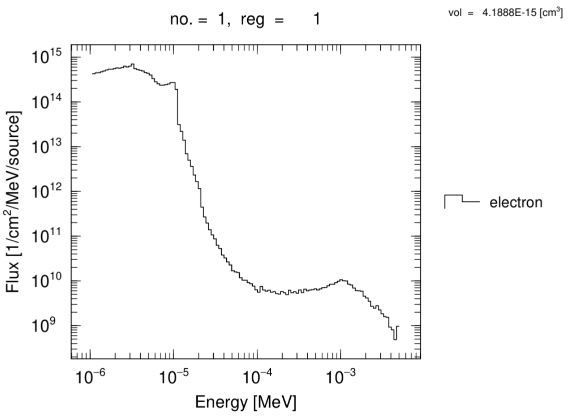

Fig. 27. 40 keV, 100 nm radius. Electron fluence spectrum.

For all configurations (Figs. 16–27), the spectrum consists of a pronounced low-energy peak around $10^{-5}$ MeV (10 eV) and a high-energy tail that includes the primary electron energy. At 1 keV, the low-energy peak reaches $\sim 10^{19}$ $\mathrm{cm}^{-2}$ $\mathrm{MeV}^{-1}$ per source in the 10 nm sphere (Fig. 16), diminishing to $\sim 10^{16}$ in the 100 nm sphere (Fig. 18), reflecting $r^{-3}$ volumetric scaling. Primary peaks are three orders of magnitude weaker, indicating a cascade of low-energy secondaries. As energy increases to 4–10 keV, the primary peak grows (e.g., Figs. 19, 22). At 40 keV in the 10 nm sphere (Fig. 25), the fluence at intermediate energies is suppressed, confirming electron escape. These spectra are crucial for evaluating track overlap and inter-track radical recombination in FLASH.

### *C. Linear Energy Transfer in Water*

Linear Energy Transfer (LET) in liquid water, denoted as let_water, is a fundamental physical quantity that describes the average energy deposited by a charged particle per unit path length. In track-structure calculations LET can be resolved event-by-event, revealing fluctuations that modulate the biological response.

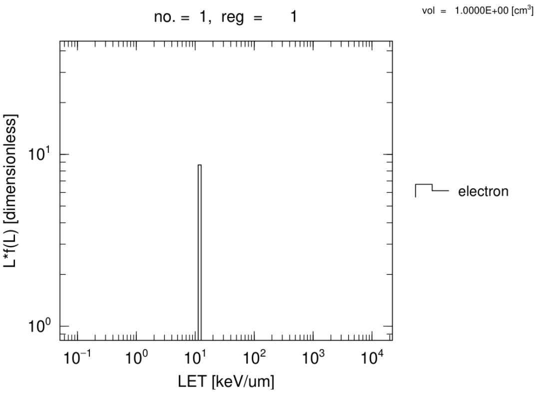

Fig. 28. 1 keV, 10 nm radius. Dose-weighted LET distribution $L \cdot f(L)$.

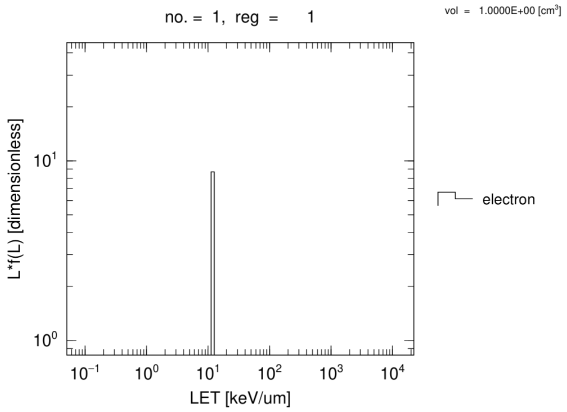

Fig. 29. 1 keV, 50 nm radius. Dose-weighted LET distribution.

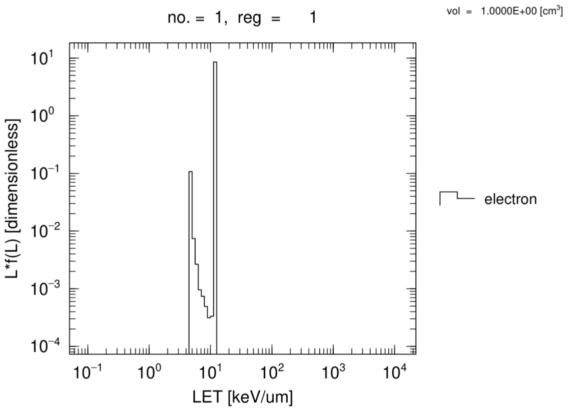

Fig. 32. 4 keV, 50 nm radius. Dose-weighted LET distribution.

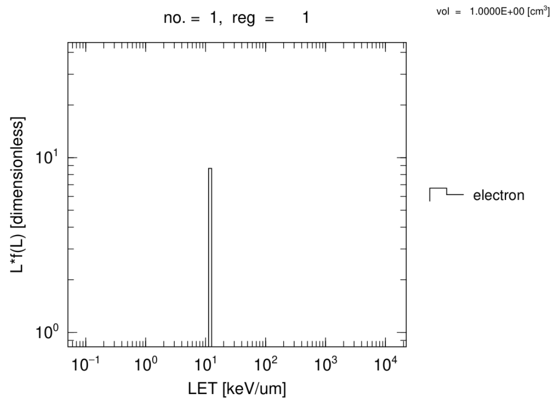

Fig. 30. 1 keV, 100 nm radius. Dose-weighted LET distribution.

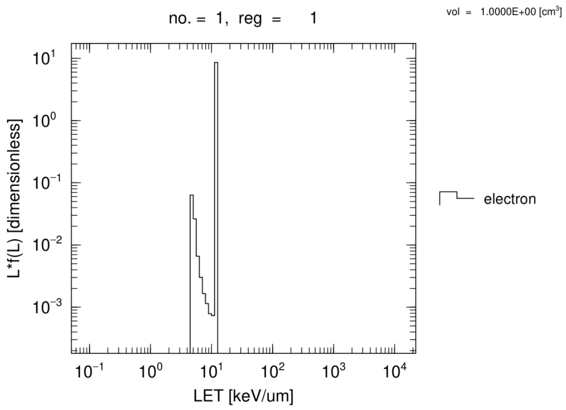

Fig. 33. 4 keV, 100 nm radius. Dose-weighted LET distribution.

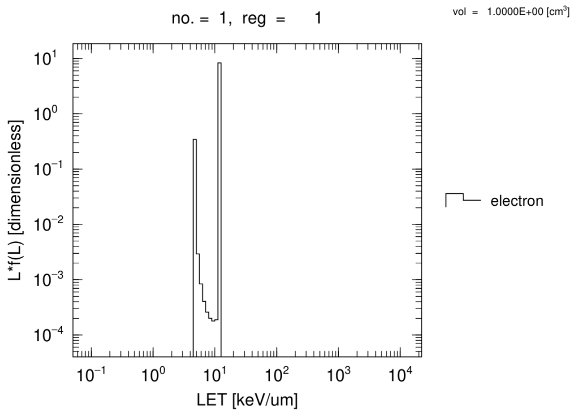

Fig. 31. 4 keV, 10 nm radius. Dose-weighted LET distribution.

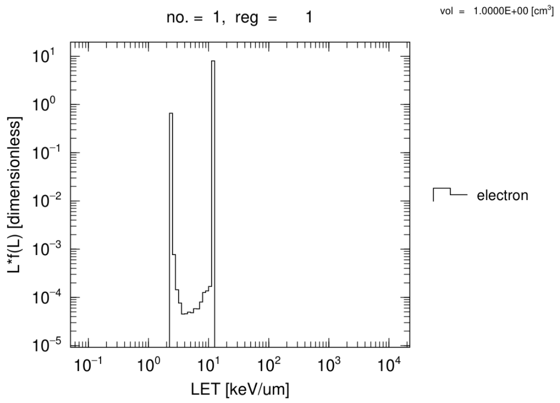

Fig. 34. 10 keV, 10 nm radius. Dose-weighted LET distribution.

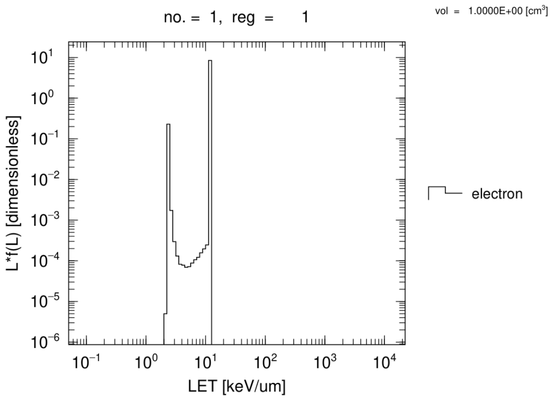

Fig. 35. 10 keV, 50 nm radius. Dose-weighted LET distribution.

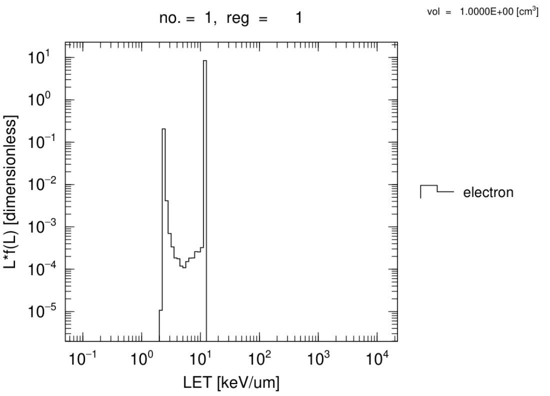

Fig. 36. 10 keV, 100 nm radius. Dose-weighted LET distribution.

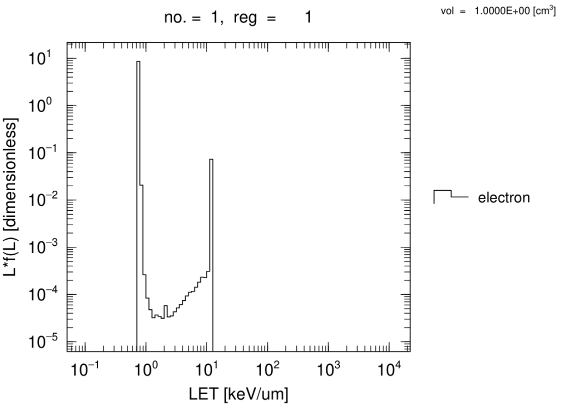

Fig. 37. 40 keV, 10 nm radius. Dose-weighted LET distribution.

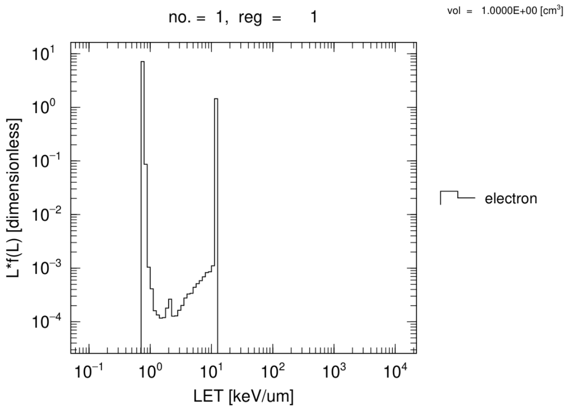

Fig. 38. 40 keV, 50 nm radius. Dose-weighted LET distribution.

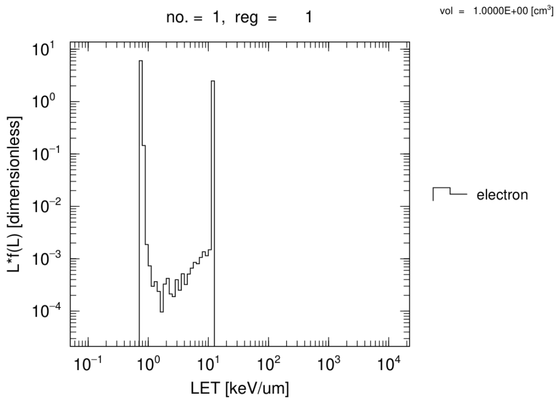

Fig. 39. 40 keV, 100 nm radius. Dose-weighted LET distribution.

The LET distributions in Figs. 28–39 measure the relative contribution of different LET values to the absorbed dose. At 1 keV, the 10 nm sphere (Fig. 28) shows a sharp high-LET peak (Bragg-peak behavior); larger spheres (Figs. 29, 30) exhibit broader spectra up to $\sim$ 100 keV/$\mu$m. At 4 keV, the 10 nm sphere (Fig. 31) narrows to $\sim$ 10 keV/$\mu$m due to electron escape; 50 and 100 nm spheres (Figs. 32, 33) extend to 50 keV/$\mu$m. At 10 keV, the 10 nm sphere (Fig. 34) narrows to $<$ 1 keV/$\mu$m, while the 100 nm sphere (Fig. 36) broadens to $\sim$ 20 keV/$\mu$m. For 40 keV, LET is $<$ 0.1 keV/$\mu$m in the 10 nm sphere (Fig. 37) and only up to $\sim$ 10 keV/$\mu$m in the 100 nm sphere (Fig. 39). These event-by-event LET spectra are essential for linking energy deposition to DNA damage complexity.

### *D. Histogram of Energy Deposition Events*

Microdosimetric spectra, represented here by the histogram of energy deposition events (edep_hist), reveal the stochastic nature of radiation interactions at the cellular and sub-cellular scales. In FLASH, the shape can indicate whether dose is delivered via many low-energy events or a few high-energy events.

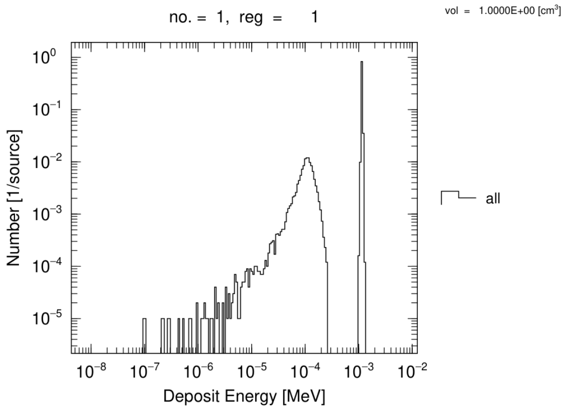

Fig. 40. 1 keV, 10 nm radius. Energy deposition event histogram.

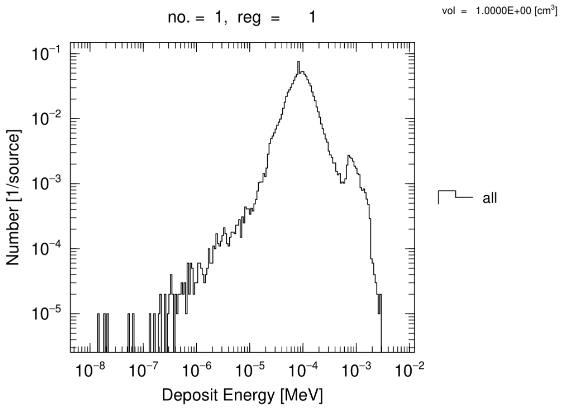

Fig. 43. 4 keV, 10 nm radius. Energy deposition histogram.

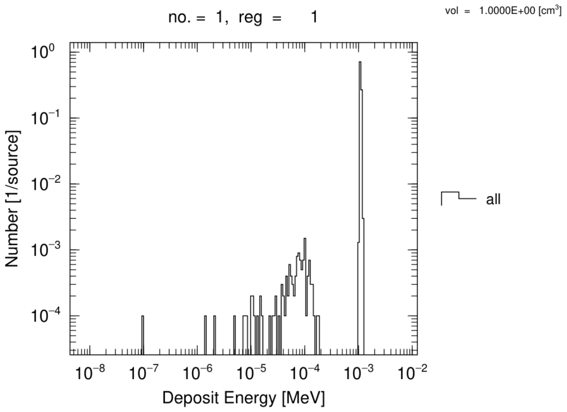

Fig. 41. 1 keV, 50 nm radius. Energy deposition histogram.

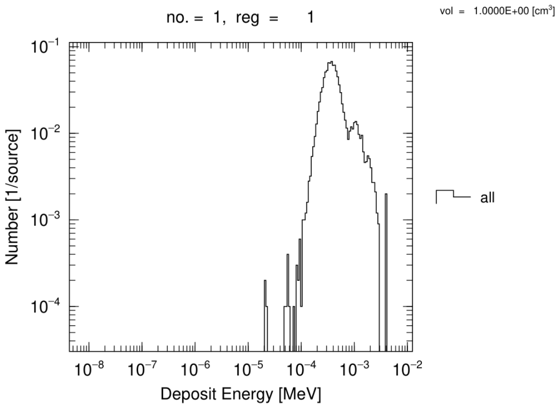

Fig. 44. 4 keV, 50 nm radius. Energy deposition histogram.

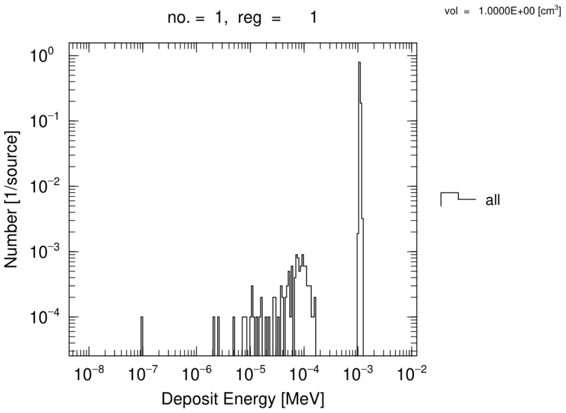

Fig. 42. 1 keV, 100 nm radius. Energy deposition histogram.

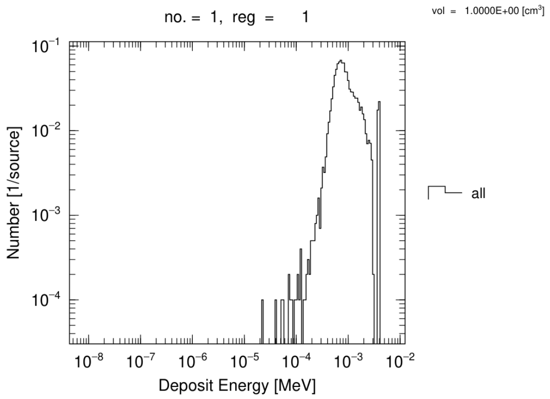

Fig. 45. 4 keV, 100 nm radius. Energy deposition histogram.

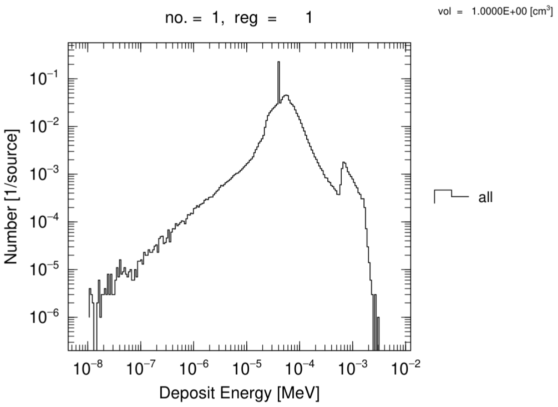

Fig. 46. 10 keV, 10 nm radius. Energy deposition histogram.

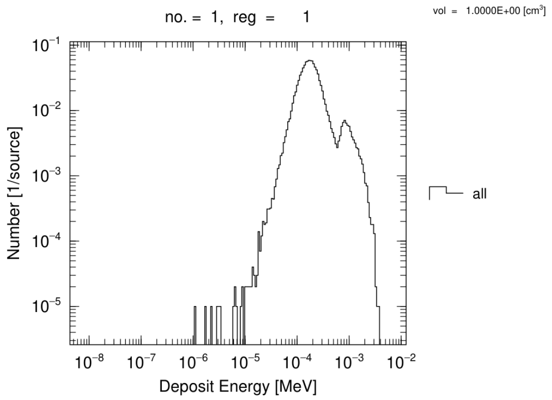

Fig. 47. 10 keV, 50 nm radius. Energy deposition histogram.

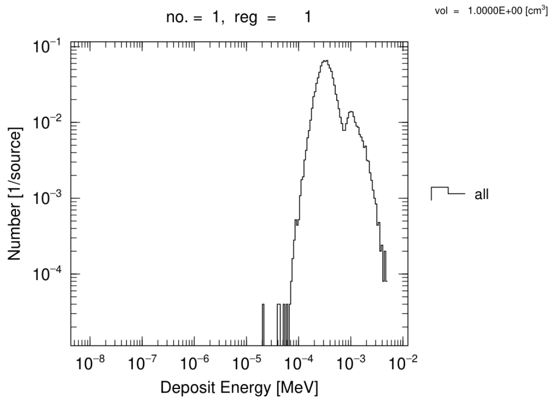

Fig. 48. 10 keV, 100 nm radius. Energy deposition histogram.

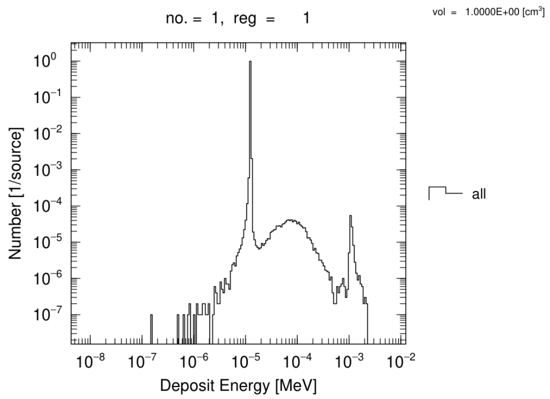

Fig. 49. 40 keV, 10 nm radius. Energy deposition histogram.

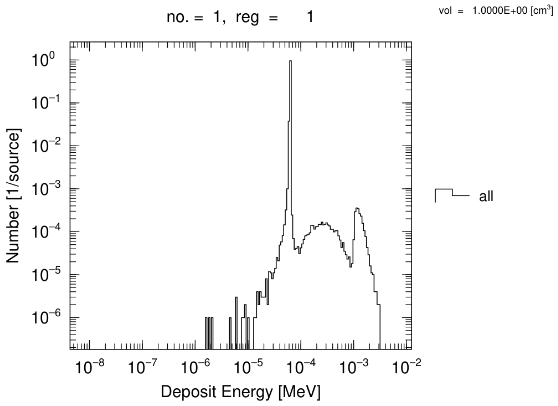

Fig. 50. 40 keV, 50 nm radius. Energy deposition histogram.

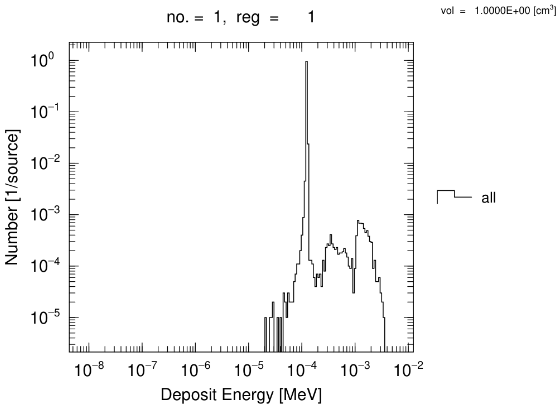

Fig. 51. 40 keV, 100 nm radius. Energy deposition histogram.

Figures 40–51 present the frequency of single energy deposition events per logarithmic energy bin. At 1 keV (Figs. 40–42), the spectra are sharply peaked near $10^{-3}$ MeV (complete energy deposition). At 4 keV, the 10 nm sphere (Fig. 43) shows a flat distribution from $10^{-8}$ to $10^{-3}$ MeV (partial depositions). At 10 keV, the 10 nm sphere (Fig. 46) is dominated by lower-energy events ($10^{-6}$˘$10^{-5}$ MeV). At 40 keV, the 10 nm sphere histogram (Fig. 49) is concentrated in the lowest bin with very low probability, indicating most electrons traverse without interaction. Broad spectra of small events (high energy, small sphere) favor sparse ionization and inter-track recombination, while peaked spectra (low energy) favor localized clusters and potentially more complex damage.

### E. Ionization Clusters

Ionization clustering is arguably the most direct physical correlate of DNA damage complexity. The ioniz_cluster analysis identifies regions where two or more ionizations occur within a few nanometers—a hallmark of a locally multiply damaged site (LMDS).

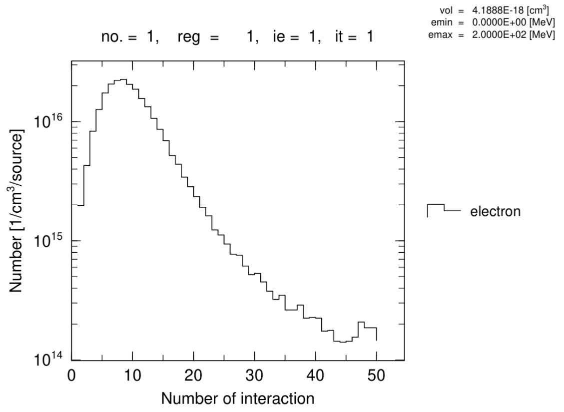

Fig. 52. 1 keV, 10 nm radius. Ionization cluster size distribution.

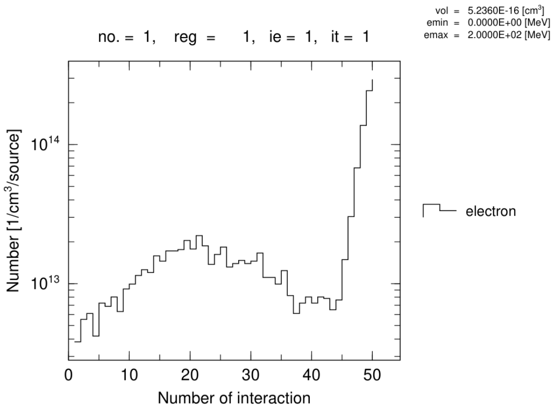

Fig. 53. 1 keV, 50 nm radius. Ionization cluster distribution.

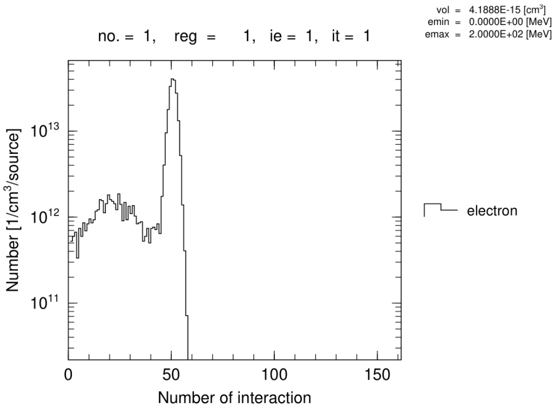

Fig. 54. 1 keV, 100 nm radius. Ionization cluster distribution.

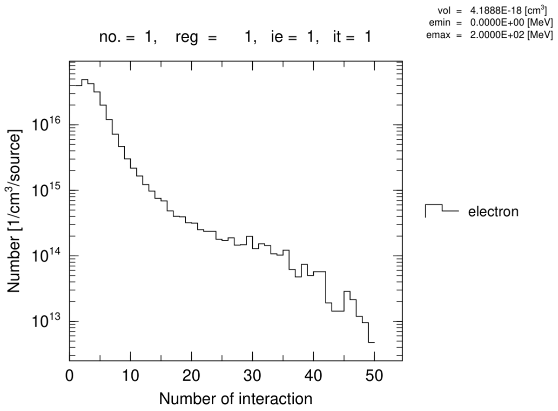

Fig. 55. 4 keV, 10 nm radius. Ionization cluster distribution.

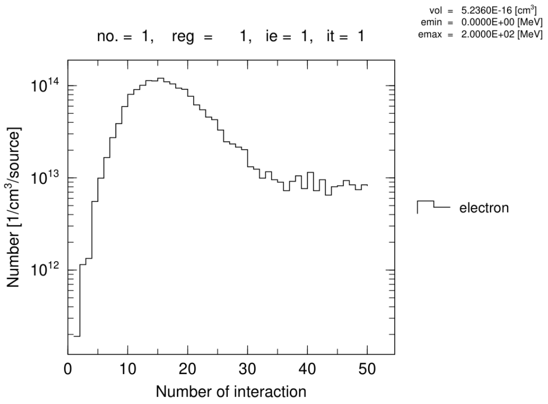

Fig. 56. 4 keV, 50 nm radius. Ionization cluster distribution.

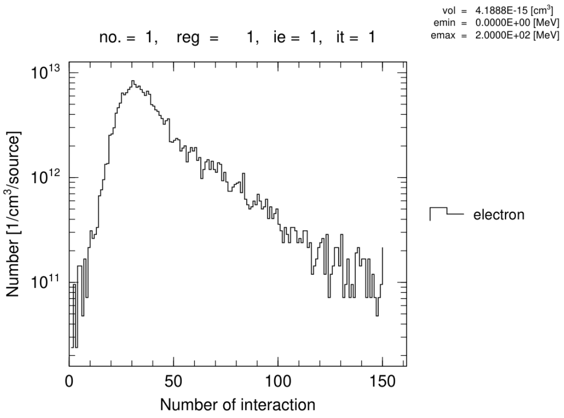

Fig. 57. 4 keV, 100 nm radius. Ionization cluster distribution.

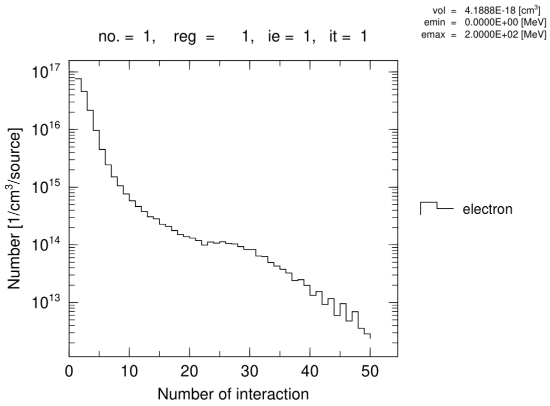

Fig. 58. 10 keV, 10 nm radius. Ionization cluster distribution.

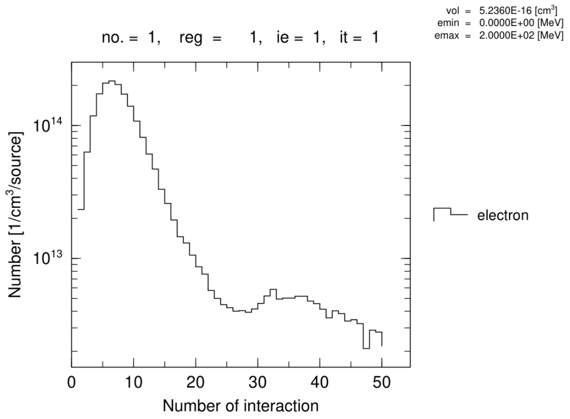

Fig. 59. 10 keV, 50 nm radius. Ionization cluster distribution.

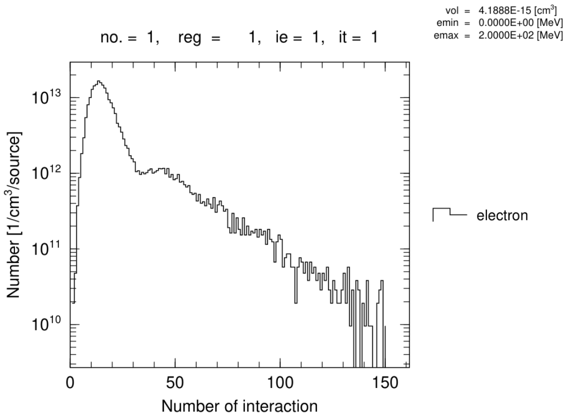

Fig. 60. 10 keV, 100 nm radius. Ionization cluster distribution.

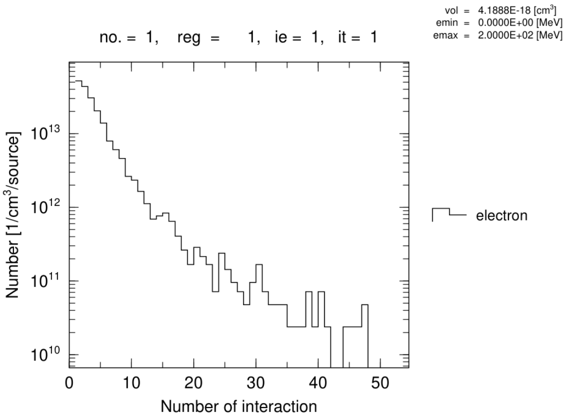

Fig. 61. 40 keV, 10 nm radius. Ionization cluster distribution.

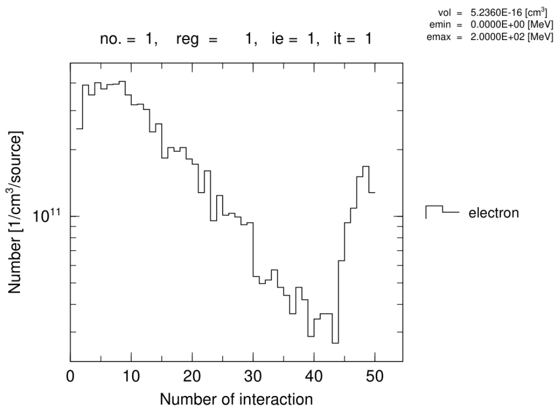

Fig. 62. 40 keV, 50 nm radius. Ionization cluster distribution.

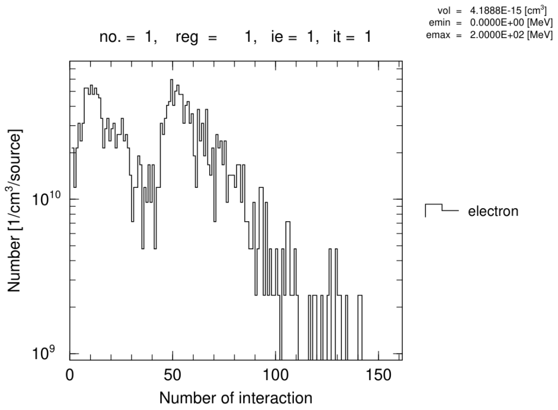

Fig. 63. 40 keV, 100 nm radius. Ionization cluster distribution.

Figures 52–63 show the probability of finding an ionization cluster of a given size. At 1 keV (Figs. 52–54), distributions are dominated by small clusters (2–4 ionizations) with frequencies $\sim 10^{15}$~$10^{16}$ cm$^{-3}$. At 4 keV, the 10 nm sphere (Fig. 55) shows virtually no clusters (escape), while the 50 nm sphere (Fig. 56) recovers to $\sim 10^{15}$ with a maximum at 12 ionizations, and the 100 nm sphere (Fig. 57) extends to 150 ionizations. At 10 keV (Figs. 58–60), similar behavior with larger clusters. At 40 keV, only clusters up to $\sim 30$ ionizations appear in the 100 nm sphere (Fig. 63), with very low probability. Large clusters correlate with complex, difficult-to-repair DNA damage. The stark contrast between small and large spheres highlights the importance of target volume in microdosimetry.

### *F. Temporal Evolution of Ionizations*

The ioniz_vs_time data set reveals the rate of ionization events during the pulse. Because ionizations directly produce hydrated electrons, hydroxyl radicals, and hydrogen radicals, the temporal density dictates the initial reactant concentration.

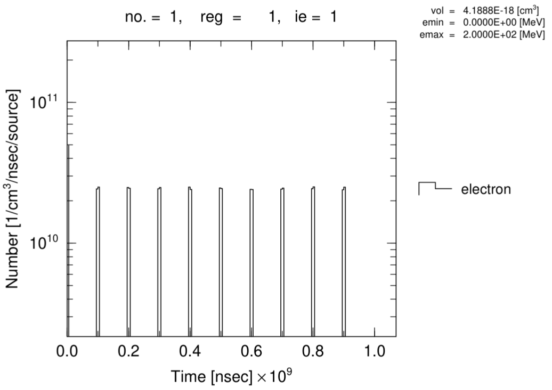

Fig. 64. 1 keV, 10 nm radius. Ionization rate vs. time.

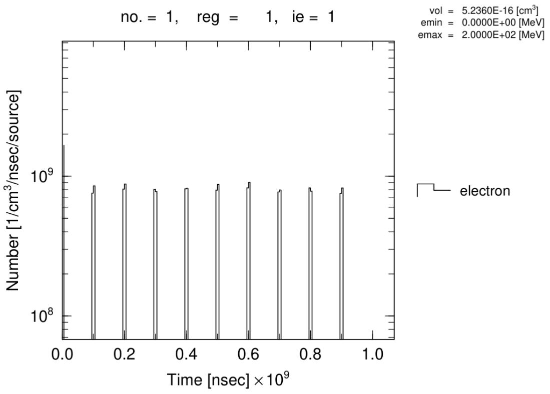

Fig. 65. 1 keV, 50 nm radius. Ionization rate vs. time.

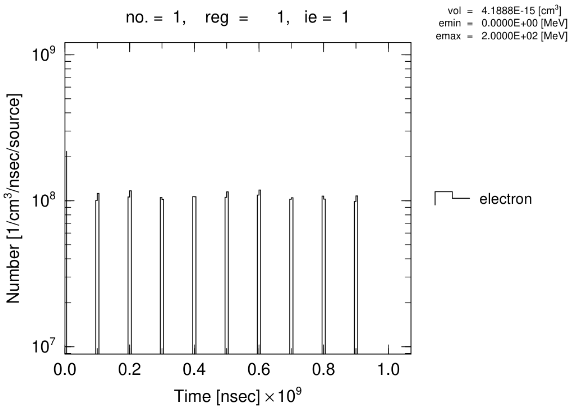

Fig. 66. 1 keV, 100 nm radius. Ionization rate vs. time.

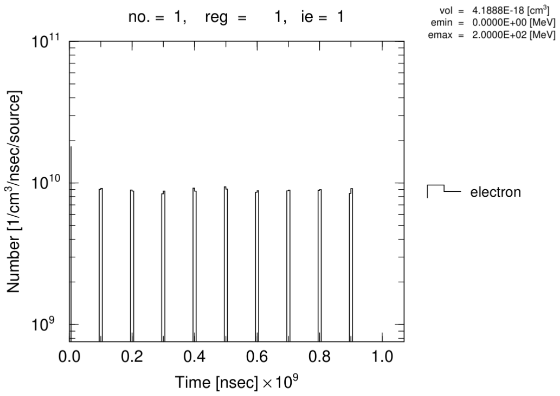

Fig. 67. 4 keV, 10 nm radius. Ionization rate vs. time.

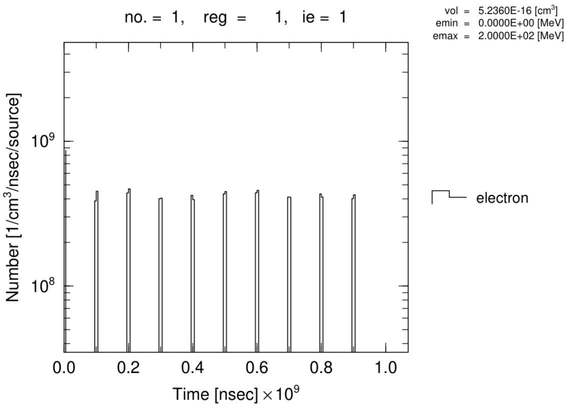

Fig. 68. 4 keV, 50 nm radius. Ionization rate vs. time.

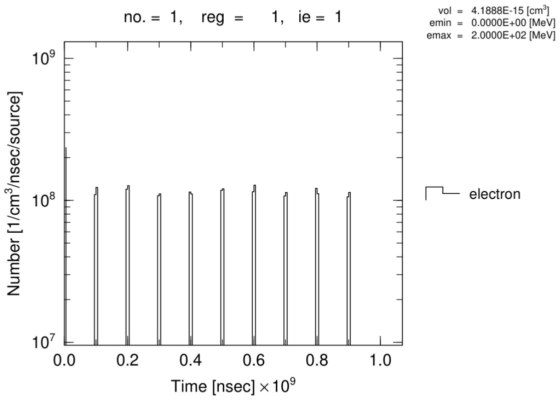

Fig. 69. 4 keV, 100 nm radius. Ionization rate vs. time.

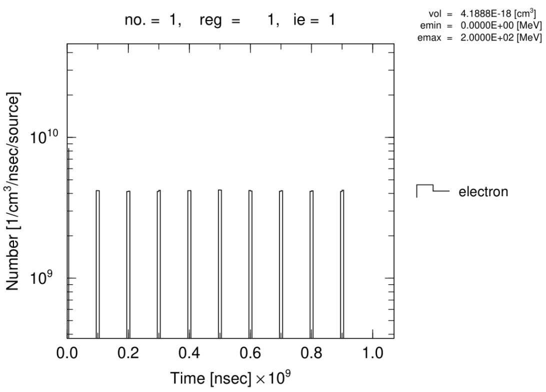

Fig. 70. 10 keV, 10 nm radius. Ionization rate vs. time.

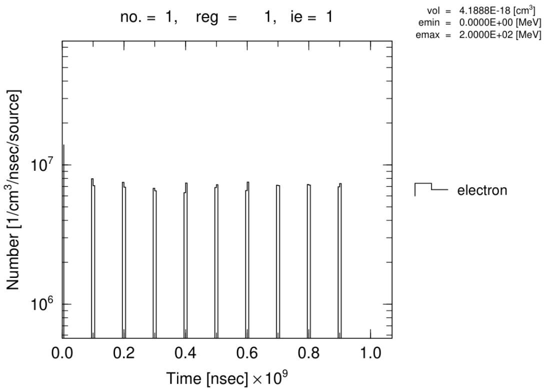

Fig. 73. 40 keV, 10 nm radius. Ionization rate vs. time.

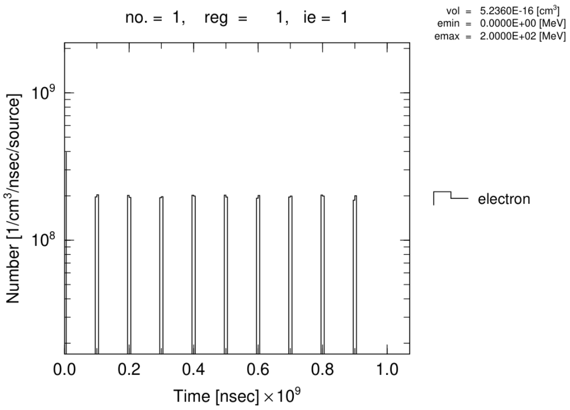

Fig. 71. 10 keV, 50 nm radius. Ionization rate vs. time.

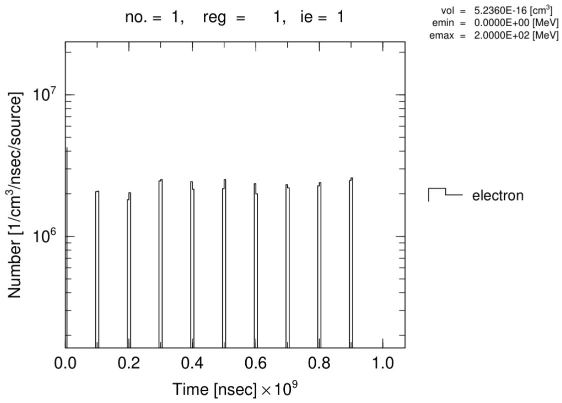

Fig. 74. 40 keV, 50 nm radius. Ionization rate vs. time.

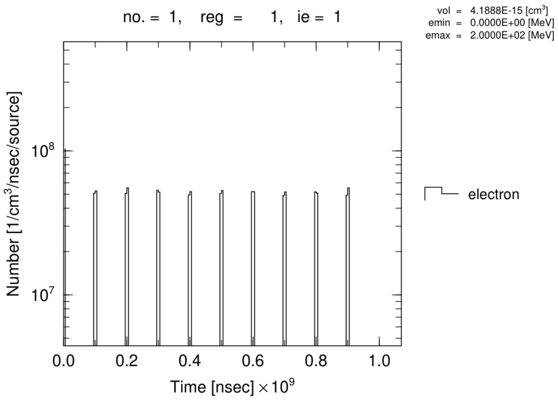

Fig. 72. 10 keV, 100 nm radius. Ionization rate vs. time.

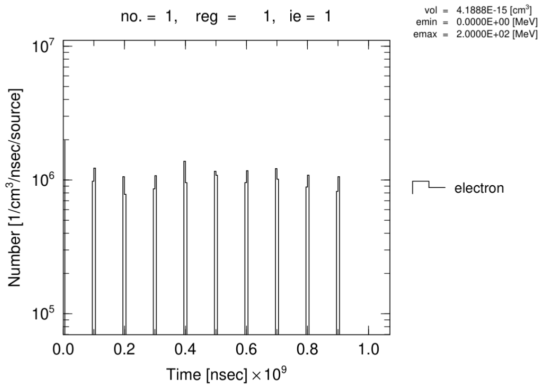

Fig. 75. 40 keV, 100 nm radius. Ionization rate vs. time.

For configurations with significant ionization (Figs. 64–75), the profile is a rectangular pulse (jump at $t = 0$, fall after 50 ns). At 1 keV, the ionization rate is $\sim 2.5 \times 10^{11}$ cm$^{-3}$ s$^{-1}$ in the 10 nm sphere (Fig. 64), dropping to $\sim 1 \times 10^8$ in the 100 nm sphere (Fig. 66). At 4 keV, the 10 nm sphere (Fig. 67) shows $\sim 2.5 \times 10^{10}$ cm$^{-3}$ s$^{-1}$. At 10 and 40 keV, the rates in the 10 nm sphere (Figs. 70 and 73) are zero (no interactions). Larger spheres (e.g., Figs. 72, 75) show rates $\sim 10^7$˜$10^9$ cm$^{-3}$ s$^{-1}$. The rectangular profile confirms that radicals are generated only during the pulse, supporting the oxygen depletion hypothesis.

## G. Electronic Excitation Clusters

Electronic excitations contribute to local energy density and can influence water radiolysis kinetics. The eexc_cluster analysis quantifies the spatial proximity of excitation events.

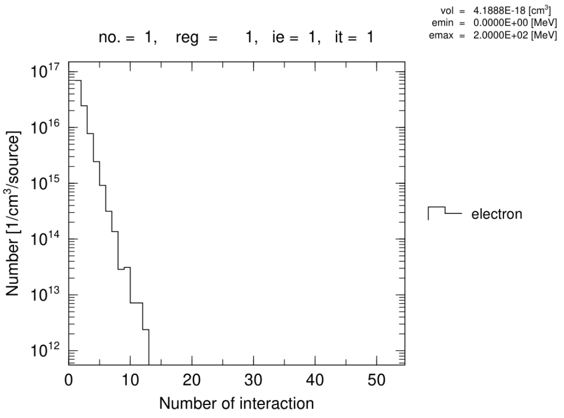

Fig. 76. 1 keV, 10 nm radius. Excitation cluster distribution.

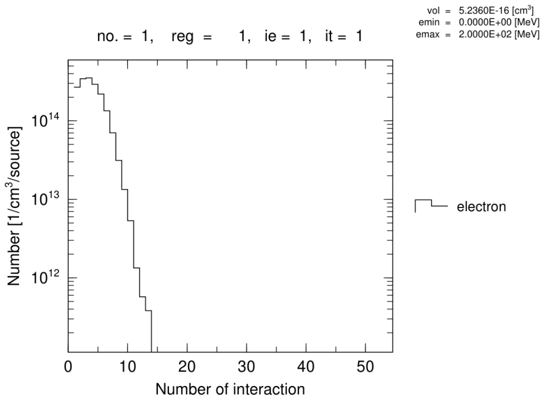

Fig. 77. 1 keV, 50 nm radius. Excitation cluster distribution.

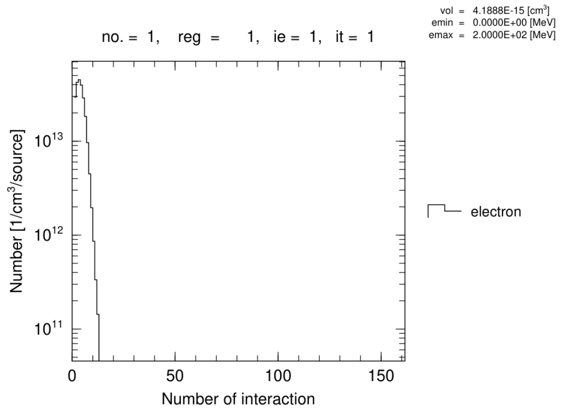

Fig. 78. 1 keV, 100 nm radius. Excitation cluster distribution.

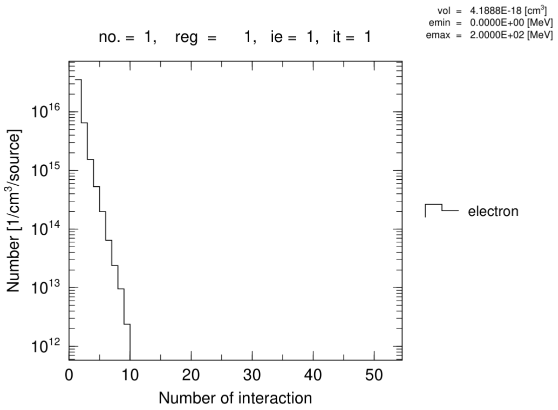

Fig. 79. 4 keV, 10 nm radius. Excitation cluster distribution.

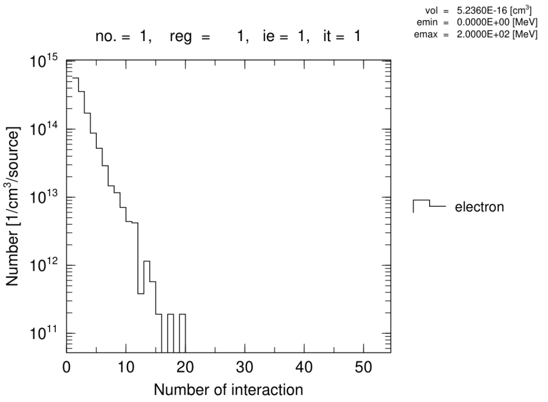

Fig. 80. 4 keV, 50 nm radius. Excitation cluster distribution.

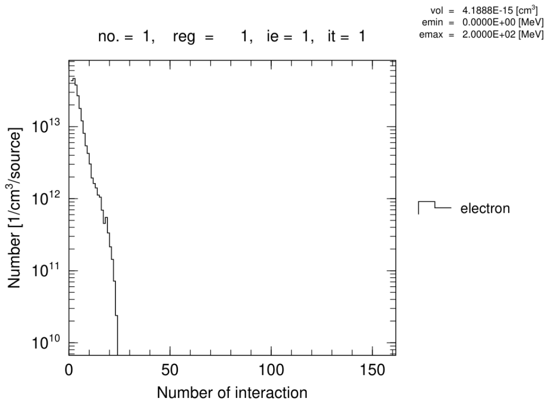

Fig. 81. 4 keV, 100 nm radius. Excitation cluster distribution.

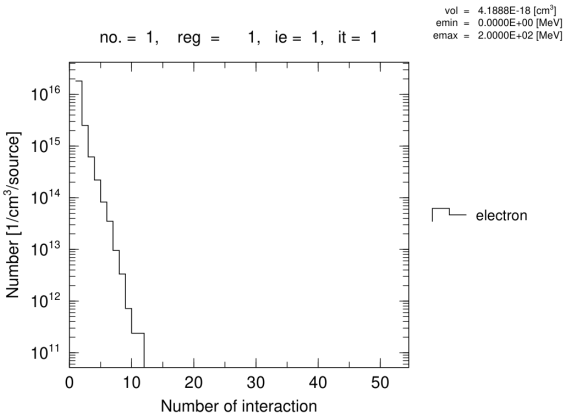

Fig. 82. 10 keV, 10 nm radius. Excitation cluster distribution.

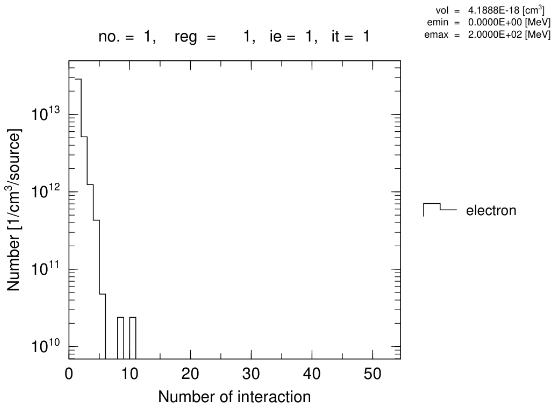

Fig. 85. 40 keV, 10 nm radius. Excitation cluster distribution.

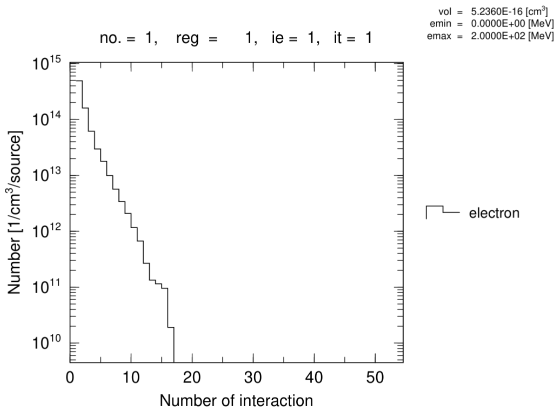

Fig. 83. 10 keV, 50 nm radius. Excitation cluster distribution.

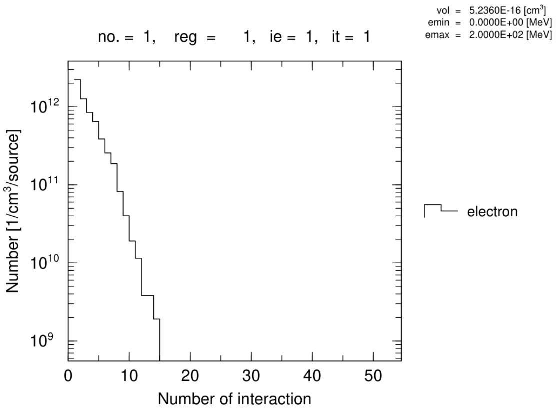

Fig. 86. 40 keV, 50 nm radius. Excitation cluster distribution.

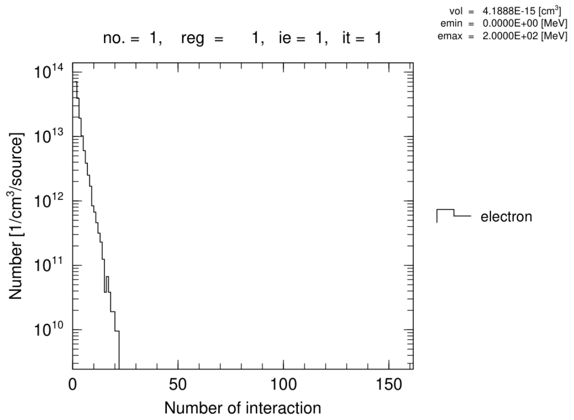

Fig. 84. 10 keV, 100 nm radius. Excitation cluster distribution.

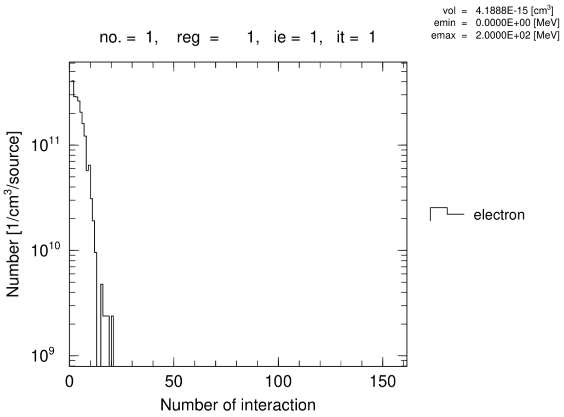

Fig. 87. 40 keV, 100 nm radius. Excitation cluster distribution.

Excitation cluster frequencies (Figs. 76–87) are generally higher than ionization clusters. At 1 keV, the 10 nm sphere (Fig. 76) shows frequencies $\sim 10^{17}$ cm$^{-3}$ for single excitations, decaying to size 50. At 4 keV, the 10 nm sphere (Fig. 79) still produces clusters up to 50 excitations with frequencies $10^{14}$~$10^{15}$. At 40 keV, excitation clusters in the 10 nm sphere (Fig. 85) are limited to sizes $< 10$ with frequencies $10^{10}$~$10^{12}$. The strong sphere-size dependence underscores the importance of target geometry for localized energy deposition and radical recombination.

### *H. Transient Biological Species Clusters*

After the physical stage, water radiolysis yields reactive oxygen species (ROS) and other free radicals (transient biological species). The tsbio_cluster analysis examines spatial correlation at the end of the chemical stage.

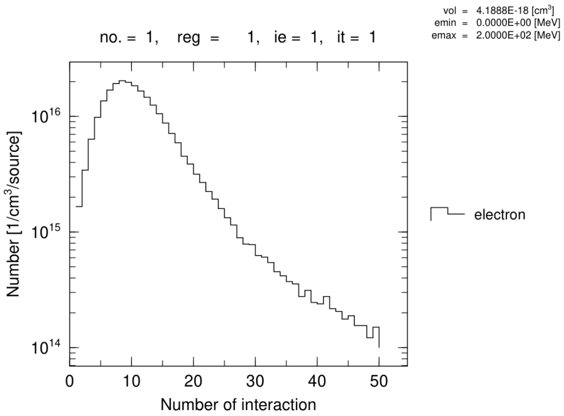

Fig. 88. 1 keV, 10 nm radius. Transient species cluster distribution.

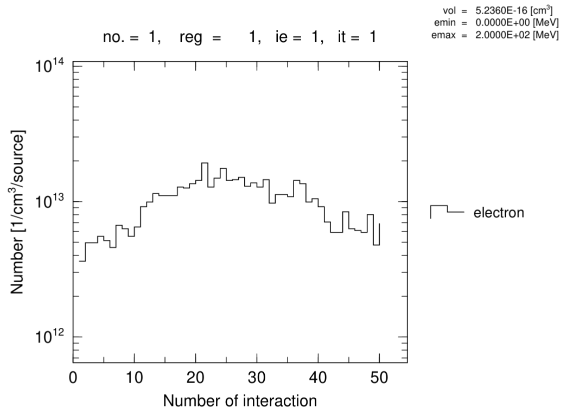

Fig. 89. 1 keV, 50 nm radius. Transient species cluster distribution.

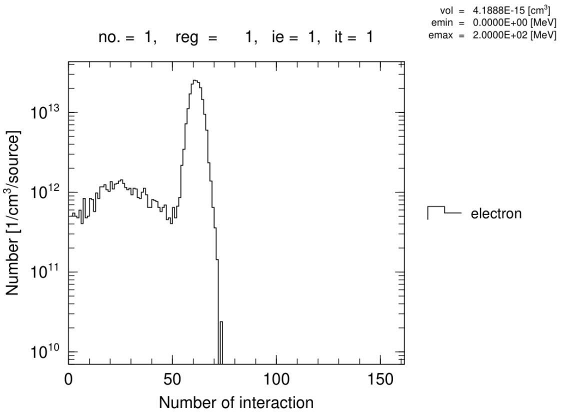

Fig. 90. 1 keV, 100 nm radius. Transient species cluster distribution.

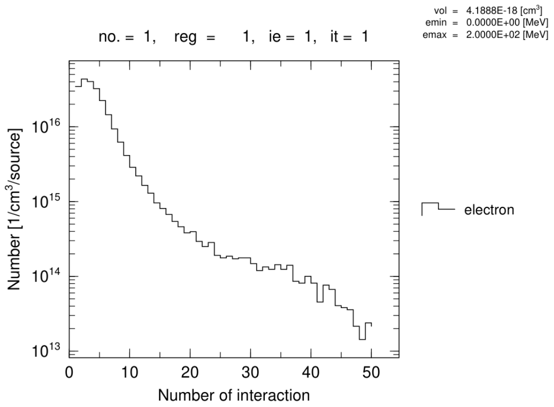

Fig. 91. 4 keV, 10 nm radius. Transient species cluster distribution.

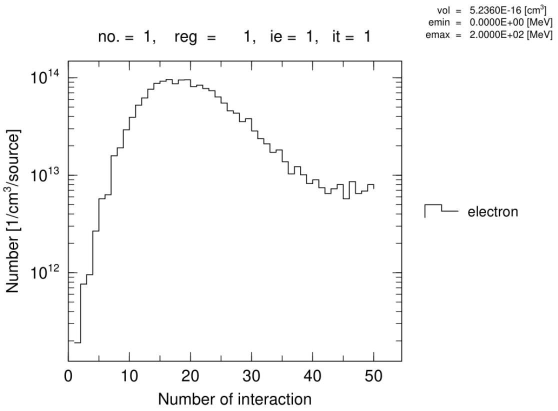

Fig. 92. 4 keV, 50 nm radius. Transient species cluster distribution.

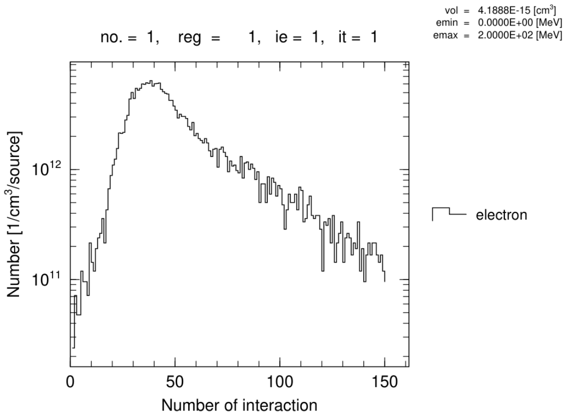

Fig. 93. 4 keV, 100 nm radius. Transient species cluster distribution.

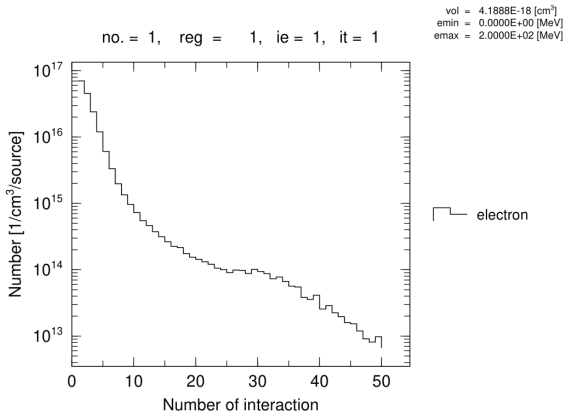

Fig. 94. 10 keV, 10 nm radius. Transient species cluster distribution.

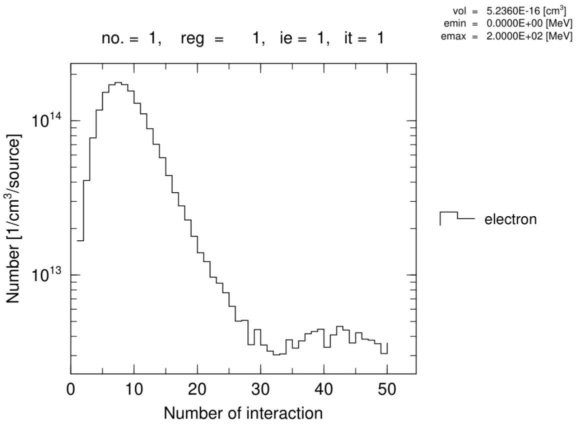

Fig. 95. 10 keV, 50 nm radius. Transient species cluster distribution.

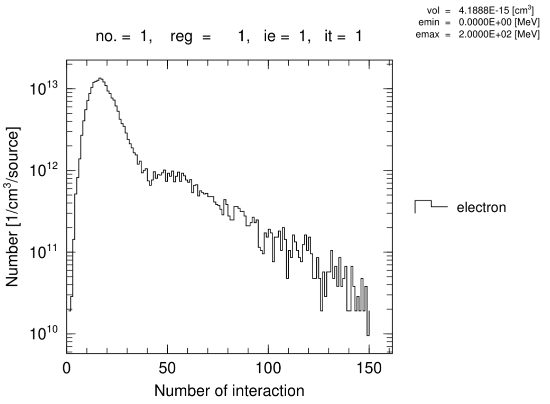

Fig. 96. 10 keV, 100 nm radius. Transient species cluster distribution.

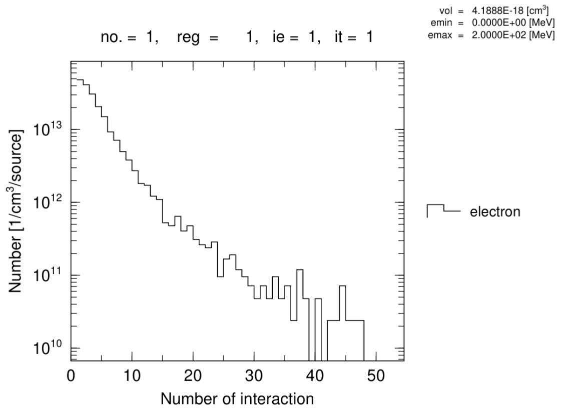

Fig. 97. 40 keV, 10 nm radius. Transient species cluster distribution.

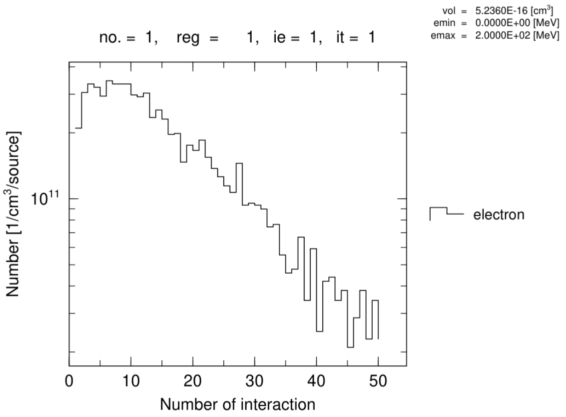

Fig. 98. 40 keV, 50 nm radius. Transient species cluster distribution.

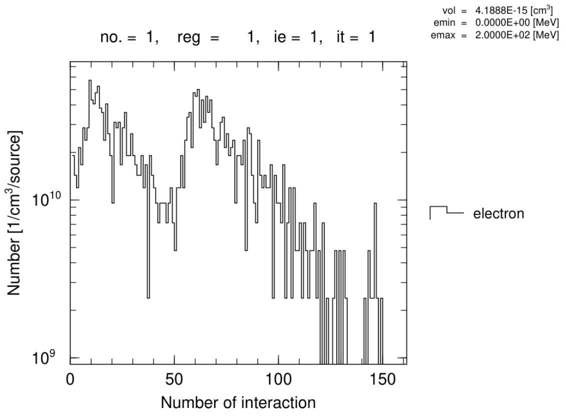

Fig. 99. 40 keV, 100 nm radius. Transient species cluster distribution.

Figures 88–99 present the spatial clustering of chemical species after 1 $\mu$s of diffusion. At 1 keV, the 10 nm sphere (Fig. 88) exhibits extremely high cluster frequencies (artifact of normalization) indicating radical concentration and local recombination. In larger spheres (Figs. 89, 90), frequencies drop. At 4 keV, the 10 nm sphere (Fig. 91) shows no clusters (no ionization/excitation), while the 50 nm sphere (Fig. 92) shows clusters rising from $10^{12}$ to $10^{20}$ for size 50. At 10 keV, again the 10 nm sphere (Fig. 94) is empty; the 50 nm sphere (Fig. 95) has a flat distribution $\sim 10^{7}$˘$10^{8}$. At 40 keV, the 10 nm sphere (Fig. 97) is empty; the 50 nm sphere (Fig. 98) shows $10^{11}$˘$10^{12}$ for small clusters. These results support the FLASH hypothesis: high local radical density favors inter-track recombination, reducing net DNA damage.

### I. Track Projection in the XZ Plane

Visual inspection of particle trajectories offers an intuitive confirmation of the simulation geometry and the stochastic nature of particle transport.

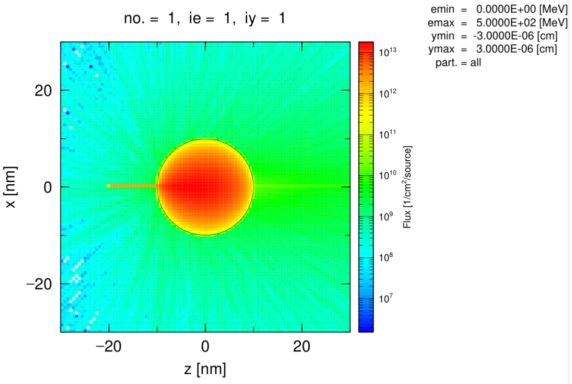

Fig. 100. 1 keV, 10 nm radius. XZ projection of electron tracks.

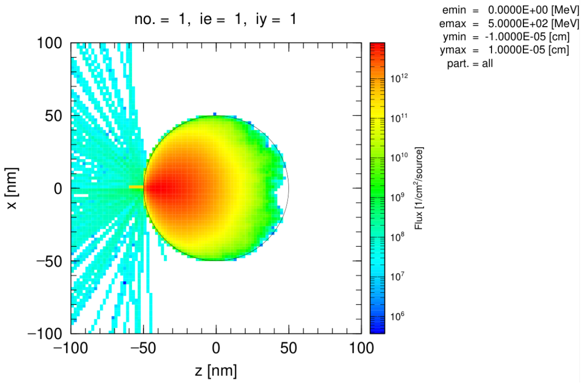

Fig. 101. 1 keV, 50 nm radius. XZ projection of tracks.

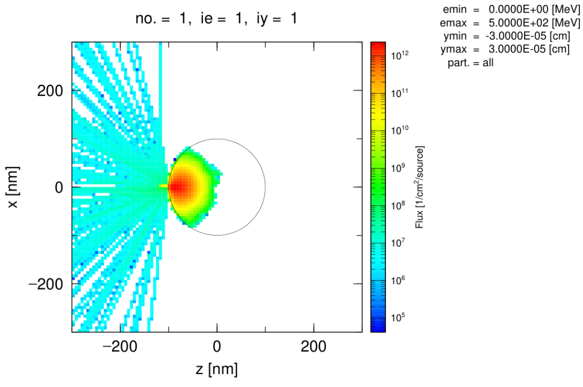

Fig. 102. 1 keV, 100 nm radius. XZ projection of tracks.

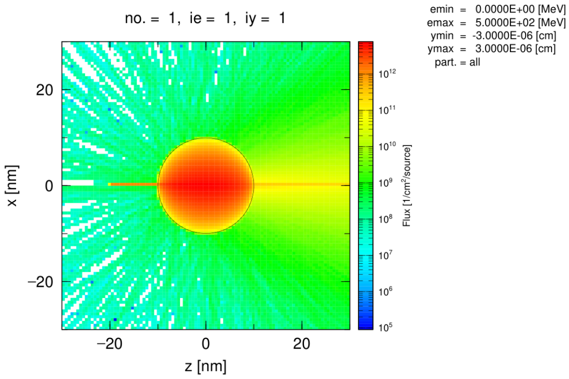

Fig. 103. 4 keV, 10 nm radius. XZ projection of tracks.

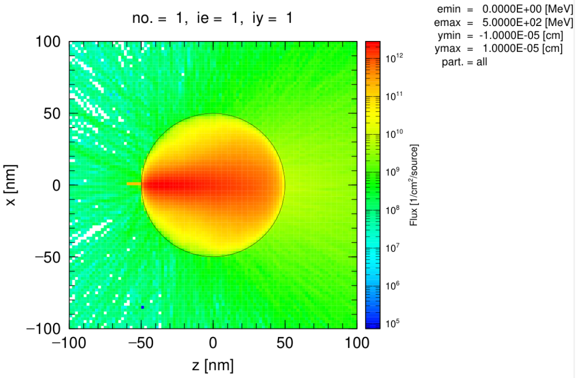

Fig. 104. 4 keV, 50 nm radius. XZ projection of tracks.

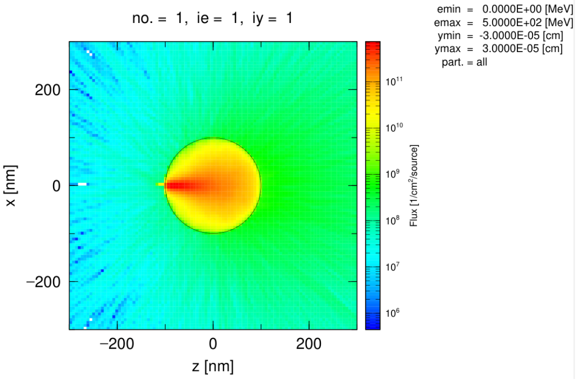

Fig. 105. 4 keV, 100 nm radius. XZ projection of tracks.

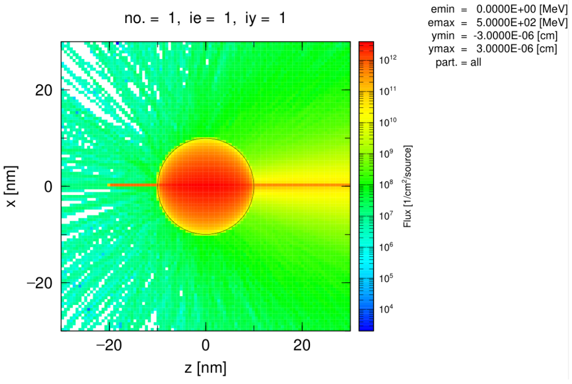

Fig. 106. 10 keV, 10 nm radius. XZ projection of tracks.

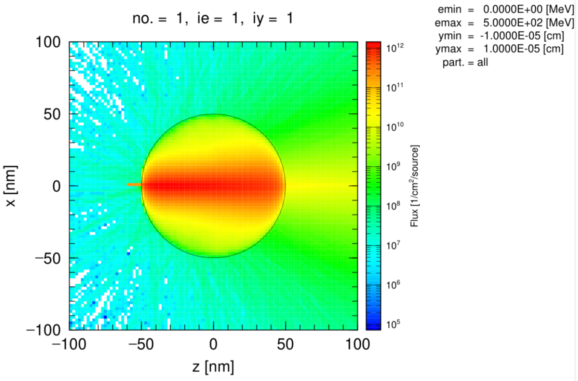

Fig. 107. 10 keV, 50 nm radius. XZ projection of tracks.

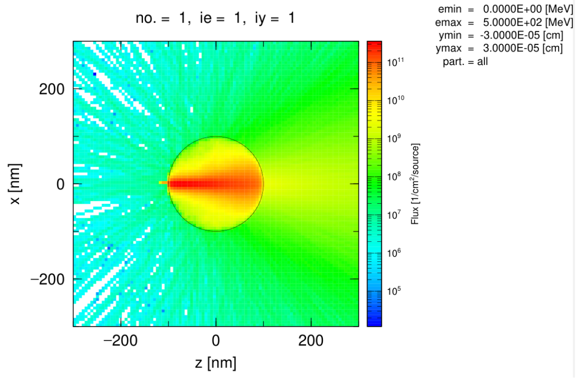

Fig. 108. 10 keV, 100 nm radius. XZ projection of tracks.

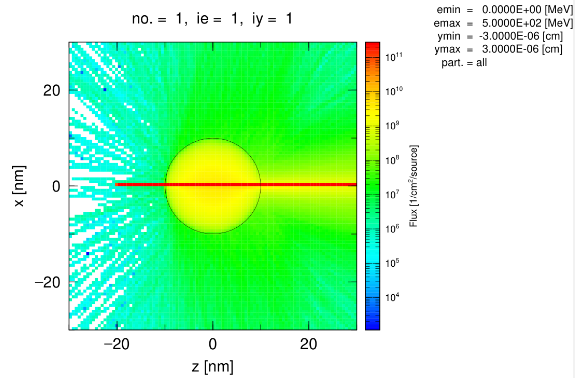

Fig. 109. 40 keV, 10 nm radius. XZ projection of tracks.

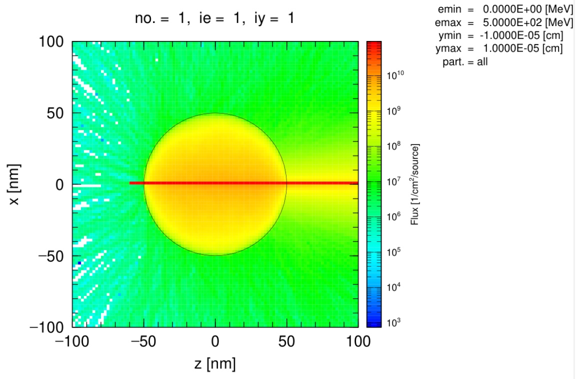

Fig. 110. 40 keV, 50 nm radius. XZ projection of tracks.

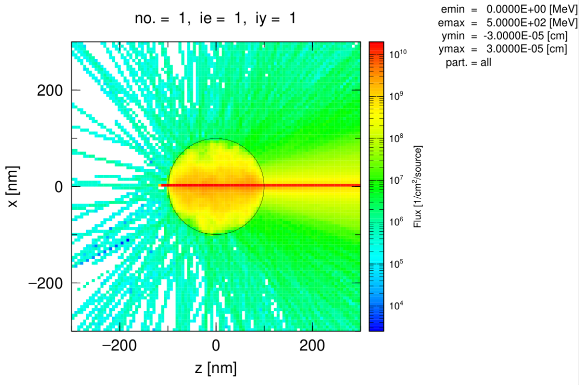

Fig. 111. 40 keV, 100 nm radius. XZ projection of tracks.

Figures 100–111 provide qualitative confirmation. At 1 keV (Figs. 100–102), dense, short tracks are fully contained in all spheres. At 4 keV, the 10 nm sphere (Fig. 103) shows some tracks exiting (faint extensions), while larger spheres contain them. At 10 keV, the 10 nm sphere (Fig. 106) shows sparse straight tracks (little energy deposition); larger spheres (Figs. 107, 108) show denser networks. At 40 keV, the 10 nm sphere (Fig. 109) shows faint straight trajectories (minimal deposition); larger spheres (Figs. 110, 111) exhibit longer, tortuous tracks. These visualizations validate the simulation and highlight the critical role of target size in determining sparse vs. dense track structures, directly affecting radical distribution and FLASH sparing effects.

## V. CONCLUSIONS

The Monte Carlo track-structure simulations carried out with PHITS and TOPAS-nBio for electron energies of 1–40 keV and biological targets of 5–100 nm allow the following conclusions:

1. The temporal profile of absorbed dose remains strictly confined to the 50 ns pulse, with no measurable delayed component, confirming that the entire energy transfer occurs during the FLASH burst. The dose per source electron scales as $r^{-3}$ for fully stopped electrons, providing a reliable normalization for microdosimetric analyses.
2. Electron fluence spectra are dominated by low-energy secondaries, whose density increases by three orders of magnitude when the target size decreases from 100 nm to 10 nm. This drastic increase in electron density underpins the high probability of track overlap, a prerequisite for inter-track radical recombination.
3. Linear Energy Transfer (LET) distributions shift from high, sharply peaked values at 1 keV to broad, lower-value spectra at higher energies and smaller volumes. The reduction of high-LET contributions in sub-100 nm targets for energies above 10 keV implies a transition from complex, clustered damage to more isolated, repairable lesions.
4. Ionization cluster analysis demonstrates that 1 keV electrons produce abundant small clusters (2–4 ionizations) independent of sphere size, whereas 4 keV electrons in a 10 nm sphere yield virtually no clusters because the incident electron escapes. The

highest probability of large clusters is obtained for 4 keV electrons in 100 nm spheres, indicating the optimal conditions for generating locally multiply damaged sites.

5. Chemical species clusters at 1 $\mu$s post-irradiation mirror the physical cluster patterns: high local radical densities in small volumes and low energies favor recombination, while sparse tracks in larger volumes or at high energies leave radicals more dispersed and available for DNA attack.
6. The escape of high-energy electrons from nanometric volumes was quantified through the reduced dose and cluster probabilities in the 10 nm sphere, directly confirming the need to account for electronic straggling when modeling dose deposition in organelles such as mitochondria or nucleosomes.

Taken together, these findings demonstrate that the FLASH sparing effect can be optimized by selecting electron energies below 10 keV and target volumes of 50–100 nm, where the combination of high track density and complete energy absorption maximizes the probability of radical recombination while minimizing the yield of complex DNA damage. The established computational platform is ready for the integration of oxygen-dependent chemistry and realistic DNA geometry in subsequent stages.

## VI. RECOMMENDATIONS

Based on the results obtained, the following recommendations are proposed to advance this line of research:

1. Extend the pulse duration parameter space to 10 ns and 100 ns in order to systematically quantify the influence of instantaneous dose rate on ionization cluster formation and radical recombination kinetics, directly testing the time-scale hypotheses of the FLASH effect.
2. Incorporate oxygen concentrations of 0.1%–21% into the PHITS chemistry module to simulate normoxic and hypoxic conditions, enabling the evaluation of the oxygen depletion mechanism at the track-structure level.
3. Integrate explicit DNA geometrical models (linear and nucleosome-wrapped DNA) into the simulations, so that the spatial correlation between ionization clusters and strand breaks can be computed directly, moving from physical descriptors to biological endpoints.
4. Perform analogous simulations with the TOPAS-nBio code and compare the resulting radiolytic yields and cluster spectra with those from PHITS, establishing a benchmark for track-structure codes in the context of FLASH radiotherapy.
5. Extend the simulations to clinically relevant electron energies (6–20 MeV) and tissue-equivalent phantoms, bridging the gap between nanoscopic track structure and macroscopic treatment planning.
6. Conduct systematic uncertainty quantification and sensitivity studies for the physical cross sections and chemical reaction rates used in the simulation, in order to assess the robustness of the predicted FLASH vs. CONV differences.
7. Finally, collaborate with experimental groups to validate the simulated G-values and microdosimetric spectra using pulsed radiolysis and fluorescent reporter systems in aqueous and cellular environments.

## ACKNOWLEDGEMENTS

This work is part of the INTEREST programme (INTErnational REmote Student Training at JINR). The authors thank the PHITS development team for their continuous support.

## REFERENCES

[1] V. Favaudon *et al.*, “Ultrahigh dose-rate FLASH irradiation increases the differential response between normal and tumor tissue in mice,” *Sci. Transl. Med.*, vol. 6, no. 245, pp. 245ra93, 2014.

[2] J. Bourhis *et al.*, “Clinical translation of FLASH radiotherapy: Why and how?,” *Radiother. Oncol.*, vol. 139, pp. 11–17, 2019.

[3] T. Sato *et al.*, “Features of Particle and Heavy Ion Transport code System (PHITS) version 3.02,” *J. Nucl. Sci. Technol.*, vol. 55, no. 6, pp. 684–690, 2018.

[4] P. Montay-Gruel *et al.*, “FLASH radiotherapy: from preclinical evidence to clinical implementation,” *Int. J. Radiat. Oncol. Biol. Phys.*, vol. 102, no. 5, pp. 1256–1268, 2018.

[5] M. Durante, J.S. Loeffler, “Charged particles in radiation oncology,” *Nat. Rev. Clin. Oncol.*, vol. 7, pp. 37–43, 2010.

[6] E. Schüler *et al.*, “Ultra-high dose rate electron beams and the FLASH effect,” *Med. Phys.*, vol. 49, no. 3, pp. 2002–2016, 2022.

[7] K. Petersson *et al.*, “DNA damage complexity as a function of radiation quality and dose rate: insights from track structure simulations,” *Radiat. Res.*, vol. 192, no. 4, pp. 413–422, 2019.

[8] P. Wardman, “FLASH radiotherapy: oxygen depletion is not the only mechanism,” *Br. J. Radiol.*, vol. 93, 20200215, 2020.

[9] J.L. Ruan *et al.*, “FLASH radiotherapy: ultra-high dose rates to spare healthy tissue,” *Nat. Rev. Clin. Oncol.*, vol. 18, pp. 339–355, 2021.

[10] H. Nikjoo, D.T. Goodhead, “Track structure analysis of ultrasoft X-rays and electrons in liquid water,” *Phys. Med. Biol.*, vol. 45, no. 4, pp. 857–871, 2000.

[11] Y. Iwamoto *et al.*, “Evaluation of track structure calculations for light ions using PHITS,” *J. Nucl. Sci. Technol.*, vol. 54, no. 1, pp. 98–107, 2017.

[12] K. Niita *et al.*, “PHITS: Particle and Heavy Ion Transport code System, version 2.23,” *JAEA-Data/Code*, 2010-022, 2010.

[13] A. Ferrari *et al.*, “FLUKA: a multi-particle transport code,” *CERN-2005-10*, 2005.